



HAL
open science

Growth and evolution of long-lived, large volcanic clusters in the Central Andes: The Chachani Volcano Cluster, southern Peru

Rigoberto Aguilar, Jean-Claude Thouret, Pablo Samaniego, Gerhard Wörner, Brian Jicha, Jean-Louis Paquette, Edwin Suaña, Anthony Finizola

► **To cite this version:**

Rigoberto Aguilar, Jean-Claude Thouret, Pablo Samaniego, Gerhard Wörner, Brian Jicha, et al.. Growth and evolution of long-lived, large volcanic clusters in the Central Andes: The Chachani Volcano Cluster, southern Peru. *Journal of Volcanology and Geothermal Research*, 2022, 426, pp.107539. 10.1016/j.jvolgeores.2022.107539 . hal-03639464

HAL Id: hal-03639464

<https://hal.univ-reunion.fr/hal-03639464v1>

Submitted on 27 Mar 2023

HAL is a multi-disciplinary open access archive for the deposit and dissemination of scientific research documents, whether they are published or not. The documents may come from teaching and research institutions in France or abroad, or from public or private research centers.

L'archive ouverte pluridisciplinaire **HAL**, est destinée au dépôt et à la diffusion de documents scientifiques de niveau recherche, publiés ou non, émanant des établissements d'enseignement et de recherche français ou étrangers, des laboratoires publics ou privés.

1 **Growth and evolution of long-lived, large volcanic clusters in the Central**
2 **Andes: the Chachani Volcano Cluster, southern Peru**

3 Rigoberto Aguilar¹, Jean-Claude Thouret², Pablo Samaniego², Gerhard Wörner³, Brian Jicha⁴,
4 Jean-Louis Paquette², Edwin Suaña⁵, Anthony Finizola^{6,7}

5 ¹ Observatorio Vulcanológico del INGEMMET, Dirección de Geología Ambiental y Riesgo
6 Geológico, Urb. Magisterial 2 B-16, Yanahuara, Arequipa, Perú (raguilar@ingemmet.gob.pe)

7 ² Université Clermont Auvergne, Laboratoire Magmas et Volcans UMR 6524 CNRS, OPGC,
8 IRD, Campus Universitaire des Cézeaux, 6 Avenue Blaise Pascal, 63178 Aubière Cedex,
9 France (j-claude.thouret@uca.fr, pablo.samaniego@ird.fr; j-louis.paquette@uca.fr)

10 ³ Georg-August Universität, Abteilung Geochemie, Goldschmittstraße 1, Göttingen, 37077,
11 Germany (gwoerne@gwdg.de)

12 ⁴ Department of Geosciences, University of Wisconsin, Madison 1215 West Dayton Street
13 Madison, WI, 53706, USA (brian.jicha@wisc.edu)

14 ⁵ Universidad Nacional San Agustín, Facultad de Ingeniería Geológica, Geofísica y Minas,
15 Arequipa, Perú (yuve04@gmail.com)

16 ⁶ Université de La Réunion, Laboratoire GeoSciences Réunion, F-97744 Saint-Denis, France
17 (anthony.finizola@univ-reunion.fr)

18 ⁷ Université de Paris, Institut de physique du globe de Paris, CNRS, F-75005 Paris, France

19
20
21
22
23
24
25
26
27
28

29 **Abstract**

30 In the Central Andes, large ($> 500 \text{ km}^2$) and long-lived (1-5 Ma) volcanic clusters (LVCs) are
31 less explored and their eruptive history and magmatic regimes less understood than smaller,
32 short-lived ($<0.5 \text{ Ma}$), individual stratocones. The Chachani-large volcanic cluster (C-LVC)
33 sizeable volume (*c.* 290 km^3) consists of twelve edifices forming the 1.06 - 0.64 Ma group of
34 stratovolcanoes and the 0.46 - 0.05 Ma group of domes coulees and block-lava flow fields. Both
35 groups overlie pre-Chachani lavas and tuffs 1.02-1.27 Ma, and together they have buried large
36 nested craters or a caldera associated with the *c.* 1.62-1.66 Ma Arequipa Airport ignimbrite.
37 The C-LVC evolved from: (i) homogeneous compositions of the pre-Chachani and Chachani
38 basal eruptive units to (ii) relatively wide compositional variations (53-67 wt.% SiO_2) between
39 mafic andesite and dacite at moderate eruptive rates ($0.27 - 0.41 \text{ km}^3/\text{ka}$) for the ‘Old Edifice’
40 group, and finally to (iii) narrower (57-64 wt.% SiO_2) andesitic compositions coinciding with
41 extrusive activity at 2.5 times lower eruptive rates ($0.12 - 0.15 \text{ km}^3/\text{ka}$) for the ‘Young Edifice’
42 group. The large compositional variations in the Old Edifice group are related to strongly
43 contrasting resident and recharge magma compositions of hybridized lavas. In contrast, the
44 narrow compositional range and lower eruption rate during the second half of the C-LVC
45 eruptive history represent a trend towards more homogeneous, andesitic magma composition
46 with time. Mineral texture and compositional studies provide evidence for disequilibrium and
47 magma mixing in the C-LVC shallow (5-20 km depth range) magma reservoirs. These temporal
48 changes in magma composition document that the transcrustal magma systems of the C-LVC
49 evolved and matured with time by a combination of processes: fractional crystallization, crustal
50 contamination and magma mixing/mingling with variable rates of mafic recharge. This resulted
51 in a shift in time to a steady state, monotonous (andesite) regime as a result of coupling between
52 compositional parameters and thermal conditions, density constraints, and the
53 viscosity/crystallinity of erupted magmas.

54 **Keywords:** volcanic cluster, petrogenesis, eruptive rate, Chachani, Central Andes, Peru

55

56

57

58

59

60 1. INTRODUCTION

61 The Central Volcanic Zone (CVZ) of the Andes is an excellent natural laboratory in which the
62 interactions between magma genesis and crustal evolution can be explored (e.g., [Wörner et al.,](#)
63 [2018](#)). These interactions have led to four main constructional volcanic types: (1) andesitic and
64 dacitic composite stratovolcanoes, (2) large volcanic clusters (LVCs) that have erupted
65 relatively wide compositional ranges from mafic andesites to dacites, (3) voluminous
66 rhyodacitic ignimbrite fields, and (4) scarce, volumetrically insignificant, basaltic or basaltic
67 andesitic, monogenic fields.

68 Studies of individual composite volcanoes in the Andean CVZ over the past 30 years have
69 provided a fundamental understanding of the eruptive behavior, timescales and magmatic
70 evolution needed to explain the variability of erupted lavas (e.g., [Wörner et al., 1988](#); [Davidson](#)
71 [et al., 1990, 1991](#); [Feeley et al., 1993, 1994](#); [Mathews et al., 1994](#); [Gardeweg et al., 1998](#);
72 [Thouret et al., 2001, 2002, 2005, 2007](#); [Gerbe and Thouret, 2004](#); [Clavero et al, 2004](#); [Delacour](#)
73 [et al., 2007](#); [Harpel et al., 2011](#); [Walker et al., 2013](#); [Godoy et al., 2014](#); [Rivera et al., 2014,](#)
74 [2017](#); [Samaniego et al., 2016](#); [Wörner et al., 2018](#); [Samaniego et al., 2020](#); [Mariño et al., 2021](#)).
75 By contrast, there are few studies on the eruptive and compositional history and thermal
76 evolution of long-lived volcanic clusters (> 1 Ma), such as the Aucanquilcha volcanic cluster
77 ([Grunder et al., 2008](#); [Klemetti and Grunder, 2007](#); [Walker et al., 2013](#)), Taápaca in northern
78 Chile ([Clavero et al., 2004](#); [Rout and Wörner, 2021](#)), and the Nevado Chachani and Nevado
79 Coropuna clusters in southern Peru ([Table 1](#)).

80 From petrological and geochemical studies at a regional scale, three end-member magmas
81 dominate andesite formation in the CVZ: calc-alkaline basaltic andesite, Sr-enriched basalt, and
82 rhyodacite ([Blum-Oeste and Wörner, 2016](#)). Highly evolved, rhyolitic magmas (>72 wt.%
83 SiO₂) rarely erupt in the CVZ from stratovolcanoes or domes; only limited rhyodacite eruptive
84 centers are found in SW Peru, such as the Purupurini dome cluster ([Bromley et al., 2019](#)), the
85 c. 34 ka-old pyroclastic deposits of El Misti cone ([Thouret et al., 2001](#); [Rivera et al., 2017](#)) and
86 the 25-9.7 ka caldera-related Plinian tephra-fall deposits of Ubinas cone ([Thouret et al., 2005](#);
87 [Samaniego et al., 2020](#)). [Wörner et al. \(2018, their Fig. 7\)](#) proposed the concept of different
88 magmatic regimes in transcrustal magma systems to better understand the variability of volcano
89 types in the Central Andes. Increasing recharge rates and decreasing volcano lifetimes
90 characterize three distinct regimes feeding CVZ polygenetic volcanoes, including: (1) long
91 lived (several My) clusters that evolve slowly from varied magmatic compositions to mostly
92 uniform dacitic lavas (e.g., Aucanquilcha cluster); (2) stratovolcanoes constructed from

93 products with a large compositional range over a short period of time (a few hundred kyr, e.g.,
94 El Misti, Ubinas, Ampato-Sabancaya), and; (3), fast growing, short-lived stratocones (e.g., 10
95 kyr “Young Cone Parinacota”) with monotonous andesitic composition. [Wörner et al. \(2018\)](#)
96 proposed that magmatic regimes can evolve, but also change back and forth from one end-
97 member to the other depending on the rate of recharge of hotter, less evolved magmas from
98 below and the size and temperature of resident, evolved magmas at shallow levels, i.e., between
99 *c.* 5 and 20 km in the upper crust. Albeit less active than iconic stratovolcanoes, LVC belie a
100 rich history of eruptive styles and epitomize the evolution of the magmatic regimes in the
101 Andean CVZ. As LVC magmas originated from depth and crossed shallow reservoirs in the
102 upper crust, unraveling the temporal changes in volume, eruption rate, and composition can
103 provide relevant information about protracted, productive transcrustal magmatic systems in the
104 Peruvian CVZ.

105 The Chachani large volcanic cluster (C-LVC) illustrates the shift between magmatic regimes
106 through its *ca.* 1.27 Myr lifetime: a relatively large compositional range from mafic andesites
107 to dacites at a moderate eruptive rate, followed by homogeneous-andesitic magmas emplaced
108 by eruptive rate 2.5 times slower, i.e., 0.12-0.15 km³/ka *versus* 0.27-0.41 km³/ka ([Tables 1-4](#)
109 and section 8.2). C-LVC may be compared with other LVCs such as Coropuna in southern Peru
110 because both developed shortly after the eruption of ignimbrites of substantial volume (20–50
111 km³) of Early Quaternary age (*c.* 1.66–1.28 Ma) with outflow sheets underlying both LVC’s.
112 Paleomagnetic measurements point to sources likely located below these clusters ([Paquereau-](#)
113 [Lebti et al., 2008](#); [Thouret et al., 2017](#); [Mariño et al., 2020](#)). We document in detail the
114 stratigraphic sequence and construction of the Chachani large volcanic cluster based on
115 analyzed magmatic compositions and new ⁴⁰Ar/³⁹Ar ages. We further propose the links between
116 this LVC and preceding medium-sized ignimbrites as a generic pattern of magma evolution in
117 LVC’s in general.

118

119 **2. LVC DEFINITION AND THE CHACHANI CASE STUDY**

120 **2.1. LVC definition and differences from other CVZ polygenetic volcanoes**

121 Large volcano clusters (LVCs) are the most voluminous constructional landforms amongst the
122 broad category of polygenetic volcanoes ([Table 1](#)) next to composite stratocones and compound
123 volcanoes ([Francis, 1993](#); [Grosse et al., 2009, 2013](#)). A LVC is defined as an extensive (250-
124 700 km²) and voluminous (200-600 km³) assemblage of spatially, temporally and genetically

125 related, clustered volcanic edifices and eruptive centers. It comprises composite and compound
126 cones with associated lava flows and pyroclastic deposits, overlapping dome complexes and
127 their coulees, as well as fissure-fed, lava-flow fields (Francis, 1993). As such, LVCs are larger
128 than typical symmetric stratocones in the CVZ ($\leq 140 \text{ km}^2$, e.g., El Misti, Parinacota; Table 1)
129 or compound volcanoes ($\leq 200 \text{ km}^2$, e.g., Ampato-Sabancaya, Taápaca; Table 1).

130 LVC's also remain active over a long ($> 1 \text{ Ma}$) period, roughly twice as long than the growth
131 period of typical individual composite or compound volcanoes (e.g., Hildreth and Lanphere,
132 1994; Hildreth et al., 2003; Singer et al., 1997; Coombs and Jicha, 2021; Table 1).
133 Exceptionally, the eruptive activity of an LVC may extend in the same area over as much as 11
134 Ma as in the case of the Aucanquilcha cluster (Klemetti and Grunder, 2007; Grunder et al.,
135 2008; Table 1). Beyond size and extended periods of activity, we argue that LVC's in the
136 Central Andes are specific in that they typically overly medium-sized ignimbrite-deposits. The
137 field and lithological relations indicate that pulses of silicic ignimbrite-forming magmas are
138 followed by slow "bleeding" of magmas with a variable range in composition from silicic to
139 mafic, again followed by a regime of more uniform hybrid intermediate andesite flows and
140 domes. So, its volume, lifetime, and the overall evolution of the magmatic regimes, distinguish
141 LVC's from other large volcanic complexes (Table 1).

142 **2.2. Structure and landform of the Chachani large volcanic cluster**

143 Extending 28.5 km from N to S and 22.5 km from W to E, the C-LVC is one of the largest
144 Andean CVZ volcanic clusters with an area of nearly 600 km^2 and an estimated maximum bulk
145 volume of $290 - 350 \text{ km}^3 \pm 10\%$ (Fig. 1, Tables 1 and 3, see Sections 4.1 and 8.1). The present
146 summit of the Chachani Volcanic Cluster at 6073 m asl is formed by the highest, and youngest
147 snow-capped 'Nevado Chachani' stratovolcano (*c.* 0.131 Ma) located 22.5-km NNW of
148 downtown Arequipa and only *c.* 15 km WNW of summit of El Misti volcano. The older volcanic
149 edifices include five more compound and composite cones, five cumulo-domes (dome
150 complexes), and widespread compound aa- and block-lava fields. The abundance of andesitic
151 lava flows and scarcity of more evolved rhyodacitic to rhyolitic pyroclastic deposits is a LVC
152 feature that has already been highlighted for the Aucanquilcha cluster (Klemetti and Grunder,
153 2007).

154 This large group of at least twelve individual edifices makes the C-LVC distinct from typical
155 and widely occurring individual stratocones (e.g., El Misti, Ubinas, Fig. 1) and from compound
156 volcanoes (e.g., Ampato-Sabancaya, Samaniego et al., 2016; Taápaca, Clavero et al., 2004;

157 [Rout and Wörner, 2021](#)) in the central Andes. Specifically, we emphasize three distinguishing
158 characteristics: (1) The large size (average basal diameter 25 km, 3 to 3.6 km total height above
159 the basement) and volume of the C-LVC exceed three- to sixfold that of typical CVZ composite
160 volcanoes (40-65 km³), including compound volcanoes (60-100 km³: [Table 1](#), and [references](#)
161 [therein](#)). This is accentuated by a wider comparison of conically shaped CVZ stratovolcanoes
162 to the LVC made by [Karátson et al. \(2012\)](#), who calculated a median of 69.1 km³ for the present
163 volume of 33 Neogene to Quaternary volcanoes in the CVZ, increasing to 88.9 km³ after
164 correction for erosion. Nine examples from their compilation exceed 100 km³, and the
165 reconstructed volume yielded 200 km³ for only three of them. Therefore, because
166 stratovolcanoes rarely exceed 200 km³, LVCs can be defined as the most voluminous volcanic
167 edifices in the central Andes (not counting, of course, large caldera complexes, de Silva and
168 Kay, 1988), e.g., C-LVC and Coropuna LVC. Magmas emplaced in the CVZ must ascend and
169 interact with a thick crust, becoming evolved, mixed and crystal-rich making difficult the
170 formation of very large stratovolcanoes/compound volcanoes as in the other volcanic settings
171 over thin crust and with an extensional tectonic regime (such as Alney-Chashakondzha in
172 Kamchatka, 207 km³; Grosse et al., 2014). Should erosion be accounted for, the initial volume
173 of C-LVC would increase by as much as 15%, that is to e.g., 333 - 397 km³ (see section 8.1).
174 (2) The *c.*1.27 My duration of volcanic activity of C-LVC indicates that its longevity is twice
175 to three times that of the CVZ individual composite volcanoes ([Table 1](#), and [references therein](#));
176 (3) Simple and compound composite cones of different age, overlapping each other, suggest
177 that eruptive activity has migrated to form two main alignments, firstly N120°E-trending over
178 *c.* 9 km for the Old Edifice group and secondly 80°E-trending over 7.5 km for the ‘Young
179 Edifice’ group. Such migration is out of proportion compared to flank eruptions feeding small
180 edifices at individual stratovolcanoes.

181 Thus, while eruptive volumes, migration of eruptive activity and longevity of LVC’s are
182 different, their compositional range from medium to high-K, calc-alkaline basaltic andesite to
183 dacite is similar to the typical compositional range of most stratovolcanoes in the CVZ.
184 However, their size and lifetime differ, and this must reflect different rates and conditions of
185 magma processing and focus on the function of transcrustal magma systems that are feeding
186 these LVCs in the CVZ.

187

188 3. GEOLOGICAL AND TECTONIC SETTING

189 **3.1. Regional geologic setting**

190 The C-LVC of Pleistocene age (≤ 1.27 Ma) belongs to the active volcanic front of subduction-
191 related volcanism in the Central Andes. It is built upon older (2.60-1.30 Ma) volcanic rocks
192 (Fig. 2) of the Early Quaternary volcanic arc (Tosdal et al., 1981; James, 1982; James and
193 Sacks, 1999; Thouret et al., 2016). The pre-volcanic basement under C-LVC and around the
194 Arequipa depression consists of two large magmatic domains, the Atico-Mollendo-Tacna
195 Domain (Coastal Batholith), and the Western Cordillera, which are separated by the Cincha-
196 Lluta-Incapuquio fault system (Fig. 3A; Vicente et al., 1982; Benavides-Caceres, 1999; Ramos,
197 2008, 2010; Carlotto et al., 2009). The Western Cordillera is formed by Neogene volcanic
198 deposits, according to the Peruvian stratigraphic nomenclature: Tacaza Group (Oligocene),
199 Huaylillas Formation (Miocene) and Barroso (Plio-Quaternary) Group (for a more detailed
200 chronostratigraphy, see Mamani et al., 2010 and Thouret et al., 2016, 2017). These volcanic
201 and sub-intrusive units cover Jurassic sediments of the Yura Group and Paleocene sediments
202 of the Huanca Formation. The basement is composed of Proterozoic high-grade metamorphic
203 rocks (the Charcani gneiss, e.g., Wilson, 1986; Ramos, 2008 and references therein).

204 Since Middle Miocene times, the Arequipa basin has been filled by a succession of ignimbrites
205 of different ages (Paquereau-Lebti, 2006, 2008; Thouret et al. 2001, 2016) (see section 5.1).
206 These ignimbrites are variably eroded and overlain by more recent volcanoclastic, alluvial and
207 glacial wash-out deposits derived from the overlying younger volcanic edifices of El Misti
208 volcano and the Chachani cluster. The close association in time and space between the Chachani
209 cluster and the youngest Arequipa Airport Ignimbrite (AAI) as well as the depositional features
210 (Fig. 3B) suggests that the C-LVC has probably been built over a caldera from which the AAI
211 was erupted (Garcia et al., 1997; Paquereau-Lebti et al., 2006, 2008). Paquereau-Lebti et al.
212 (2008) measured anisotropy of magnetic susceptibility (AMS) and componentry that confirm
213 that the source of the AAI sheet was located underneath the C-LVC. The 13 km long, N-S
214 oriented, arcuate scarp 9 km to east of Chachani has been interpreted from satellite images as
215 the possible rim of the proposed “Chachani caldera” (Fig. 3B; Garcia et al., 1997). The AMS
216 measurements, however, did not provide evidence for the source location of the Río Chili and
217 La Joya ignimbrites, so RC and LJ sources are poorly constrained but presumed to be
218 somewhere on the Altiplano beyond El Misti volcano and near the Sumbay valley northeast of
219 the C-LVC (Paquereau-Lebti et al., 2008).

220 **3.2. Transpressional tectonic regime in oblique convergent margin**

221 The active continental margin has long been described as the result of archetypal Andean
222 subduction (Thorpe, 1982; Wilson, 1986; Stern, 2004), which, in southern Peru, has developed
223 by oblique convergence (Ramos, 2010; Armijo et al., 2015). The present-day range of arc
224 volcanoes, located 220-250 km east of the Peru-Chile Trench and above a 30° dipping slab,
225 formed upon the Western Cordillera (Figs. 2 and 3A). The maximum compressive stress (σ_1 =
226 N80°E) is accommodated by N130°E and N160°E strike-slip faults at least since Cenozoic
227 times (Mering et al., 1996; Sempere and Jacay, 2006, Sempere et al., 2014). The transpressional
228 tectonic regime affects the SW flank of the Western Cordillera at the northern edge of the
229 Arequipa basin, as sketched in Figure 3C. The WNW-ESE-trending Arequipa depression has
230 been interpreted as a pull-apart basin at the intersection of ~N130°E strike-slip and normal
231 faults, and N10° and N40° faults (Mering et al., 1996; Thouret et al., 2001, Benavente et al.,
232 2017). The active, N130°E strike-slip faults parallel the Western Cordillera, e.g., the Ayo-Lluta-
233 Arequipa and Río Chili faults that cut the SE flank of Chachani and El Misti stratocone, and
234 the Aguada Blanca fault on the East side of C-LVC. The Western Cordillera parallels active,
235 normal and strike-slip N130° faults, while the oblique N80°E convergence is accommodated
236 by en-echelon N160°E faults (Fig. 3C).

237 Individual arc volcanoes like El Misti, Ubinas, and Chachani straddle the faulted flank of the
238 Western Cordillera on the northern edge of the pull-apart basin of Arequipa (Gonzales et al.,
239 2014). As a result of the pull-apart basin in transpressional setting, N80°-trending, active normal
240 faults cut the flank of the Western Cordillera in a series of staircase looking south (Figs. 3A and
241 5). This asymmetry likely has implications on edifice growth, alignment and migration of vents,
242 and potential edifice instability due to the steeply SW-ward dipping base (Fig. 3C).

243 The C-LVC has been built up in a complex structural setting (Figs. 3A-C, 5). A group of edifices
244 in the north and east are aligned along reverse and strike-slip N160°E faults (Figs. 3A and 4);
245 whereas, in the central part of the C-LVC, a group of edifices has grown along N80°E-trending
246 structures that cut out staircases looking south in the folded, Mesozoic sedimentary rocks of the
247 Western Cordillera (Figs. 3A and 4). These staircase structures of the south WC flank looking
248 south appear on 2D diagrams (Fig. 6) that help reconstruct the approximate pre-Chachani
249 palaeo-topography. On the south flank of the C-LVC, the Airport-Potrero dome-coulee
250 complex and several small vents are aligned along N10°E and N40°E open eruptive fissures
251 that fed extensive aa and block-lava fields to the south and SW (Fig. 3A).

252

253 **4. METHODS**

254 **4.1. Geological mapping and sample collection**

255 The geological map (Fig. 4) was compiled from preliminary fieldwork carried out by Suaña
256 (2011) and our additional fieldwork, coupled with interpretation of SPOT5 (2.5 m pixel) and
257 Google Earth satellite images. Satellite imagery and SRTM-based DEM-shaded reliefs enabled
258 us to define and delineate the position and elevation of contacts between the C-LVC and its
259 inclined base around the volcano and inside the Río Chili canyon to the east. Individual volcanic
260 edifices of the C-LVC were distinguished based on observed morphological, erosional, and
261 angular discordances. The location of visible craters and vents and uniform surface
262 morphologies and satellite image colors further allowed us to delineate twelve individual
263 volcanic edifices comprising the C-LVC. In several cases, it was also possible to identify, lower,
264 middle and upper stratigraphic units within a volcanic edifice based on observed overlap, inset
265 landform relations, and stratigraphic unconformities that allowed us to separate different stages
266 of lava flow eruptions. Edifice boundaries and stratigraphic units were embedded in a GIS-
267 based 1:25,000 scale topographic map. Sub-units have been labeled using the first three letters
268 of the edifice name, followed by a number pointing to its stratigraphic position (e.g., Noc1 is
269 the basal unit of the Nocarane edifice; Fig. 4).

270 Based on our new geologic map and the 30-m SRTM DEM data, we calculated the total volume
271 of the C-LVC with three different tools and techniques. We used (1) Surfer® and (2) ArcMap®
272 software to perform a difference between the DEM elevation (actual topography) and the 3-D
273 reference basal surface beneath the C-LVC (topography without the C-LVC; more details in
274 section 8.1). Additionally, we computed the volume using (3) MORVOLC algorithm (Grosse
275 et al., 2012).

276 During fieldwork, representative samples of lavas were collected for petrographic and
277 geochemical analysis. Samples for the radiometric dating were taken specifically from the base
278 and top units of the volcanic edifices in order to best constrain the period of activity of each
279 edifice.

280 **4.2. Analytical methods**

281 **4.2.1. Mineralogy and geochemistry**

282 Thin sections of fifty-two fresh samples allowed us to describe most of edifice lavas of the C-
283 LVC. Given that the mineral assemblage is rather homogeneous, the number of samples is
284 thought to be representative. Major element composition for main mineral phases of fourteen

285 representative samples were analyzed at the Laboratoire Magmas et Volcans (LMV), Université
286 Clermont Auvergne (Clermont-Ferrand, France) using a Cameca SX-100 electron microprobe
287 (See ESD Table 2). The most representative textures were analyzed to recognize composition
288 changes during crystal growth and infer petrogenetic processes. For geochemical analyses,
289 sixty-eight samples were crushed and milled in an agate mortar. For major element analysis,
290 powdered samples were mixed with LiBO₂, placed in a graphite crucible, and melted in an
291 induction oven at 1050°C for 4.5 min, resulting in a homogeneous glass bead. The glass was
292 then dissolved in a solution of deionized water and nitric acid (HNO₃) and finally diluted by a
293 factor of 2000. The final solutions were analyzed by ICP-AES (Jobin-Yvon ULTIMA C) at
294 LMV. Trace element analyses have been carried out by ICP-MS at the Centre de Recherche
295 Pétrographiques et Géochimiques in Nancy, France. These new data were combined with
296 previously analysed rock samples from Chachani reported in Mamani et al. (2010).

297 **4.2.2. Dating techniques**

298 *⁴⁰Ar/³⁹Ar geochronology*

299 Alkali feldspars (average K/Ca= ~ 1) were isolated from pyroclastic rocks and groundmass /
300 glass separates were prepared via magnetic and density separation using methylene iodide. All
301 purified separates were weighed and then irradiated at the Oregon State University TRIGA
302 reactor in the Cadmium-Lined In-Core Irradiation Tube (CLICIT). ⁴⁰Ar/³⁹Ar incremental
303 heating experiments were undertaken on groundmass/glass separates following Jicha et al.
304 (2012). Single crystal fusions were performed on the feldspar separates following the methods
305 of Meyers et al. (2012). Argon isotope analyses were done using a MAP 215–50, and the data
306 was reduced using ArArCalc software version 2.5 (<http://earthref.org/ArArCALC/>). All age
307 data presented here are calculated relative to 28.201 Ma for FCs (Kuiper et al., 2008), the decay
308 constants used are those of Min et al. (2000), and the age uncertainties reported in Table 2
309 reflect only analytical contributions at the 2σ level.

310 *La-ICP-MS U-Pb geochronology*

311 U-Th-Pb isotopic data on separated zircons were obtained by laser ablation inductively coupled
312 plasma spectrometry (LA-ICP-MS) at LMV. The analyses involved the ablation of minerals
313 with a Resonetics M-50 Excimer laser system operating at a wavelength of 193 nm coupled to
314 a Thermo Element XR Sector Field ICP-MS. Spot diameters of 33-44 were associated to
315 repetition rates of 3 Hz and fluency of 3 J/cm². The analytical method for isotope dating, U-Pb
316 fractionation and mass bias corrections and quality control is basically similar to that reported

317 in [Hurai et al. \(2010\)](#), [Paquette et al. \(2014\)](#), and [Mullen et al. \(2018\)](#). Data reduction was
318 carried out with the software package GLITTER[®] from Macquarie Research Ltd ([van
319 Achterbergh et al., 2001](#)). ²³⁰Th disequilibrium was corrected according to [Schärer \(1984\)](#).
320 Concordia ages and diagrams were generated using Isoplot/Ex v. 2.49 software package by
321 [Ludwig \(2001\)](#). The zircon analytical results were projected on ²⁰⁷Pb/²⁰⁶Pb versus ²³⁸U/²⁰⁶Pb
322 diagrams ([Tera and Wasserburg, 1972](#)).

323 ⁴⁰Ar/³⁹Ar ages indicate cooling in groundmass (i.e., eruption ages) whereas U/Pb indicate
324 crystallization age of the analyzed zircon crystals. Considering their uncertainties, there are no
325 age discrepancies between chronology and stratigraphy for main groups of edifices. Thus, we
326 used these dates to constrain the temporal evolution by distinguishing chrono-stratigraphic
327 intervals of edifices into a long-lived system such as the C-LVC. However, our age, volume
328 and eruption-rate estimates have high uncertainties when it comes to individual edifices. Similar
329 dating methods were used to correlate the stratigraphy of Neogene and Quaternary ignimbrites
330 in southern Peru ([Thouret et al., 2016](#)). Table 2 indicates the two different groups of ⁴⁰Ar/³⁹Ar
331 data with (1) exponent and U/Pb data with (2) exponent. ESD Table 3 displays analytical data
332 for ⁴⁰Ar/³⁹Ar ages.

333

334 **5. ERUPTIVE CHRONOLOGY**

335 **5.1. Pre-Chachani: ignimbrites and lava flows**

336 The bedrock of the C-LVC consists of a series of rhyolitic ignimbrite sheets described by
337 [Paquereau-Lebti et al. \(2006, 2008\)](#) and volcaniclastic deposits that crop out in the Arequipa
338 basin and the Río Chili canyon ([Figs. 4 and 5](#)).

339 1. The Río Chili ignimbrite ('Chuquibamba' c. 13.12–13.19 Ma; [Thouret et al., 2001, 2016](#))
340 exposed at the base of the Río Chili canyon overlying older strata displays a massive, up to 140
341 m thick cooling unit, with non-welded to partially welded crystal-rich deposit.

342 2. The La Joya ignimbrite 'LJI' (c. 4.86-4.89 Ma; [Paquereau-Lebti et al., 2006](#)) filled the
343 Arequipa basin and mantled part of the Arequipa Batholith to the SE of the basin.

344 3. The Arequipa Airport Ignimbrite 'AAI' (20-25 km³) consists of two units with weighted
345 mean ages of 1.66 ± 0.07 Ma for the lower white unit and 1.62 ± 0.04 Ma for the upper pink
346 flow unit ([Paquereau-Lebti et al., 2006, 2008](#)). The source of these ignimbrites is not exposed
347 but is thought to be buried below the C-LVC. This is indicated by anisotropy directions of

348 magnetic susceptibility measurements and the size of lithic fragments contained in the upper
349 AAI pink unit, which increases northward towards Chachani (Paquereau-Lebti et al., 2008).
350 The upper AAI unit is overlain by a 1.41 ± 0.25 Ma old pyroclastic density current (PDC)
351 deposits close to Nevado Chachani (e.g., Cerro Colorado, airport area; Paquereau-Lebti, 2006).

352 4. A series of black, vesiculated and plagioclase-rich lava flows crops out in the La Paccha
353 riverbed at the west margin below younger lavas from Nocarane stratovolcano (Fig. 4). These
354 lavas are overlain by the Yura tuffs (YT) and therefore these lavas are considered to form the
355 local bedrock of Quaternary age.

356 5. The Yura Tuffs ‘YT’ (Jenks, 1948) are a series of non-welded ignimbrite deposits with
357 intercalated layers of reworked volcanoclastic deposits. The YT (1.5 km^3) have been $^{40}\text{Ar}/^{39}\text{Ar}$
358 dated at 1.28 ± 0.05 Ma (on plagioclase) and 1.03 ± 0.09 Ma (on biotite; Paquereau-Lebti et al.,
359 2006). YT deposits are restricted to the north and west sides of the C-LVC, filling a north-south
360 elongated depression between the sedimentary ‘Yura’ Group of Jurassic age (Wilson and
361 García, 1962) and the Pre-Chachani lava bedrock (Fig. 3A). The source of the YT lies below
362 the lava flows of the Baquetane volcano north of the C-LVC.

363 6. Deposits of the Capillune Formation (Guevara, 1969) overlap the La Joya Ignimbrite to the
364 east of C-LVC. Based on the stratigraphic position below Pre-Chachani lava flows and
365 geochemical correlations (Paquereau-Lebti et al., 2008) with the Yura tuffs, the Capillune Fm.
366 may be of similar age, i.e., between 1.63 Ma and 1.28 Ma. A 20-km-wide depression suggests
367 the existence of an older caldera of Plio-Quaternary age (Garcia et al., 1997), now filled by 10
368 to 30 m-thick sequence of non-welded pyroclastic flow and tephra-fall deposits intercalated
369 with lacustrine deposits of the early Pleistocene Capillune Fm to the east of C-LVC and north
370 of El Misti volcano (Fig. 3A), and ignimbrites of the *c.* 4.86-4.89 Ma LJI (Paquereau-Lebti et
371 al., 2006).

372 **5. 2. Volcanic evolution of C-LVC**

373 We distinguish two groups of ‘Old Edifice’ and ‘Young Edifice’ and investigate to which extent
374 the C-LVC and earlier ignimbrite magmas in the same area may be related. Based on 1:25,000
375 scale mapping, identification of structural growth patterns and stratigraphic relationships,
376 together with twenty $^{40}\text{Ar}/^{39}\text{Ar}$ and U/Pb ages (Figs. 4 to 6, Table 2), we reconstruct the eruptive
377 chronology of the C-LVC, which is characterized by recurrent activity and short periods of
378 quiescence.

379 **5.2.1 Old Edifice group lavas (*c.* 1280–640 ka)**

380 The early Pleistocene Old Edifice group was built between *c.*1280 and 640 ka and form the
381 eastern and northern parts of the C-LVC (Table 2). The largest individual volcanic structures
382 (Nocarane, Estribo and Chingana) and the smaller El Colorado dome coulees follow a N150°-
383 N160° arcuate trend.

384 *The C-LVC basal lava flow unit*

385 The initial activity of C-LVC produced andesitic lava flows that cover an area of 25 km² and
386 represents a volume of 1.33 - 3.62 km³ (Fig. 4, Table 2). The lowest unit was directly emplaced
387 onto the YT on the NW side of the C-LVC, but middle and upper units are intertwined with the
388 YT. The second unit of lava flows on the SW flank of the C-LVC overlies a thin unit of alluvium
389 deposits just above the upper unit of the AAI. The age of these basal flows therefore is between
390 *c.*1280 ka (Yura Tuff age) and *c.* 1010 ka (i.e., the onset of the overlying Chingana edifice).

391 *Chingana stratovolcano*

392 Located on the NE side of the C-LVC, Chingana (44 km², 32.10 - 47.40 km³) is the oldest
393 exposed stratovolcano of the cluster. Lavas exposed at its base (U/Pb age of 1012 ± 53 ka, Table
394 2) reached a distance of 7 km from the vent. The flanks were partly buried by the younger
395 Nocarane and El Angel edifices. The middle unit is made up of andesite ⁴⁰Ar/³⁹Ar dated at 916
396 ± 41 ka (Table 2). The upper unit of Chingana consists of basaltic andesite lava flows that are
397 the least silicic (53.68 wt.% SiO₂) of all observed C-LVC lavas.

398 *Nocarane stratovolcano*

399 The 121 km², 65.53 - 125.93 km³ and 5760 m-high Nocarane stratovolcano, dated between *c.*
400 916 and 641 ka (Table 2), consists of a thick pile of andesite lava flows topped by lava domes.
401 Three overlapping units include: (1) the lower unit on the NW part of the edifice that consists
402 of scoria deposits (Noc1) and dark lava flows with restricted tephra-fall deposits (Noc2-Noc4).
403 (2) Block-lava flows and domes were emplaced on the top and towards the NNW flank. An
404 andesitic dome, now glaciated, was emplaced at high elevation (5400 m) just north of the
405 summit (Noc10) and yielded a U/Pb age of 866 ± 71 ka (Table 2). (3) The morphologically
406 most recent flow forms the summit plateau at 5748 m asl (undated). A flat dome in the middle
407 of the 500 m-wide cirques at the summit open to the west is also still partly preserved and could
408 represent a glacially eroded crater fill. On the lower flanks, a succession of dark gray lava flows
409 extends to NE as far as ~9.3 km (Noc11–Noc14). One of these andesitic lavas (Noc15) on the
410 lower western flank was ⁴⁰Ar/³⁹Ar dated at 754 ± 10 ka, which represents the youngest dated
411 unit of Nocarane. Based on our dating and the similar morphology of all flows on the lower

412 flanks of Nocarane, the period of activity of this volcano was rather short and restricted between
413 870 and 750 ka. This age range largely overlaps with dates from Estribo and Colorado centers
414 (see below and [Table 2](#)) and thus marks a time of focused andesite eruptions at C-LVC.

415 *Estribo stratovolcano*

416 This sizeable stratovolcano (120 km² and 59.35 - 63.03 km³) is located on the SE edge of C-
417 LVC ([Fig. 4](#)). Since Río Chili has cut a canyon into the base of the C-LVC and the bedrock at
418 the SE margin of Estribo, it exposes older Early Quaternary ignimbrites, a 200-300 m thick
419 volcanoclastic succession of unknown origin, and the earliest pyroclastic deposits and lava flows
420 sourced from the Estribo center. Later, this canyon was partly filled by middle Pleistocene
421 debris-avalanche deposits from Estribo ([Bernard et al., 2017](#)). The base of Estribo exhibits
422 volcanoclastic sediments overlain by hydroclastic deposits ([Fig. 4](#), HR in [Fig. 5A](#)) that contain
423 decimeter-sized glassy breadcrust bombs and associated breccia and lapilli tuffs with
424 intercalated, coarse, normally graded pumice-fall layers. These deposits were partly
425 palagonized after wet deposition and are probably related to sub-glacial eruptive processes.
426 These deposits are conformably overlain by subaerial block-lava flows of the middle Estribo
427 unit.

428 The volcanoclastic succession below the Estribo deposits overlies the 1.62 Ma upper pink-unit
429 of the AAI as well as the 1.40 Ma PDC and tephra-fall deposits that are exposed west of
430 Arequipa ([Thouret et al., 2001](#); [Paquereau-Lebti et al., 2006](#)). The pyroclastic sequence includes
431 intercalated tephra and PDC deposits in channel fills ([Wegner and Ruprecht, 2003](#)) and thins
432 out towards the SE below the oldest Estribo and El Misti lava flows. Distally to the SW, this
433 volcanoclastic succession encompasses lahar deposits intercalated with pumice-fall deposits and
434 thins out towards the basin of Arequipa. Debris-avalanche and lahar deposits suggest that
435 erosion and collapse affected the earliest C-LVC edifices towards the Arequipa depression.
436 This volcanoclastic fan therefore suggests a depositional period of intertwined eruptive activity
437 possibly from a “palaeo-Estribo” volcano and other Old Edifice group located below the
438 younger Chachani edifices. Their facies indicate extensive interactions between volcanic and
439 glacial activity and their age falls between the older dated ignimbrite eruptions (1.40 Ma) and
440 the base of Estribo (c. 746-871 ka). As such, these deposits represent the earliest post-caldera
441 products between the formation of the underlying older ignimbrites and the initiation of eruptive
442 activity of the present C-LVC edifices ([Fig. 5](#)).

443 The earliest lava flows of the Old Edifice group from the basal unit of Estribo consist of
444 andesitic and dacitic lavas (Est1–Est5) that flowed down ~10 km to the south of Estribo’s
445 summit. A pronounced angular unconformity located at about 4800 m distinguishes the lower
446 from middle units. The middle unit consists of andesite lava flows and scoria-fall and flow
447 deposits (Est6). One flow of the upper units of this eruptive center (Est8) is 808 ± 63 ka
448 ($^{40}\text{Ar}/^{39}\text{Ar}$) old, while the most recent lava flow (Est10) is 694 ± 75 ka ($^{40}\text{Ar}/^{39}\text{Ar}$). Andesitic
449 lava flows that extend ~10.4 km to the NE of the vent partly covers deposits of the Chingana
450 stratovolcano. These Estribo flows overlap in age with a lava flow exposed at the base of El
451 Misti on its lower W flank and across on the northern side of Río Chili canyon, which was dated
452 at 833 ± 6 ka (Thouret et al., 2001). This flow had previously been considered to be a precursor
453 to El Misti volcano (≤ 112 ka). However, with the new ages of C-LVC and the observed
454 stratigraphic relations, this lava flow is more likely part of the Estribo edifice.

455 *El Colorado dome coulees*

456 El Colorado (12.3 km^2 and $4.13\text{-}6.16 \text{ km}^3$) is the northernmost composite dome-coulee complex
457 of the C-LVC. It has been built by extrusive pulses of two superimposed porphyritic andesite
458 domes coulees $^{40}\text{Ar}/^{39}\text{Ar}$ dated at 642 ± 88 ka on the WNW lower flank of Nocarane
459 stratovolcano. At the top of the highest dome coulee, a breached vent, now occupied by a dome,
460 was the vent for a lava flow that propagated 2.2 km to the northeast and overlapped the two
461 domes coulee units. The subdued but preserved, ropy lava flow surface is consistent with the
462 relatively young age compared to the other the Nocarane flows and thus represents the most
463 recent event of the Old Edifice lavas of the C-LVC.

464 **5.2.2 Young Edifice group lavas (c. 460–56 ka)** A series of younger, Middle to Late
465 Pleistocene edifices is aligned south and SW of the Old Edifice group. The Young Edifice lavas
466 have built a 12.5-km long edifice that now forms a glaciated WSW-ENE ridge (N80°E) across
467 the south-sloping pre-Chachani basement (Figs. 3, 4). Extrusive activity of the Young Edifice
468 group has produced abundant cumulo-domes, dome coulees and block-lava flow fields, which
469 are morphologically better preserved compared to the Old Edifice group. Their vents are aligned
470 along the N80°E ridge formed by these edifices, while the Cabrería dome vents (~56 ka, Table
471 2) are also aligned N80°E on the southern flank of Estribo stratovolcano.

472 *El Angel stratovolcano*

473 El Angel is a small stratovolcano (~ 13 km^2 , $4.86 - 5.56 \text{ km}^3$) made up of a succession of four
474 andesite lava flows (Ang1–Ang4). Two craters are still visible on the top of the edifice which

475 has been eroded to the west flank over which the younger Chachani summit lavas were
476 emplaced. To the E, lavas have covered the youngest lavas of Chingana and Estribo
477 stratovolcanoes. Zircons from a lava unit covered by Nevado Chachani stratovolcano were
478 U/Pb dated at 463 ± 34 ka. As El Angel is morphologically better preserved and shows at least
479 ~200 kyr difference with surrounding edifices (Chingana and Estribo), which is not observed
480 in both groups' eruptive hiatus, this stratocone may be the earliest of the aligned Young Edifice
481 group of the C-LVC.

482 *Airport-Potrero dome cluster*

483 Dome-coulees and stubby lava flows form a prominent, complex landform between 5 and 15
484 km SW of the summit of Chachani. This dome complex shows both large areal extent (*c.* 68
485 km²) and volume (between 11.22 and 12.53 km³). Single, up to 100 m thick and stubby block-
486 lava flows issued from a cluster of dome-coulees. The lower and middle units of the Airport-
487 Potrero dome cluster dated by ⁴⁰Ar/³⁹Ar at 397 ± 40 ka (PD1) and 369 ± 62 ka (PD3),
488 respectively, consist of porphyritic lavas with composition straddling the boundary between the
489 andesite and dacite fields (62–64 wt.% SiO₂, Fig. 8). The middle unit (PD 4-7) also consists of
490 dacite, whereas the upper unit lavas (PD 8-10), ⁴⁰Ar/³⁹Ar dated at 292 ± 5 ka, shows a silicic
491 andesite composition. The uppermost unit (undated) shows a 1.8 km-sized ring-shape
492 subsidence in the central part affecting the most recent dome coulees. A series of craters are
493 aligned along N10°-40°E and N130°E eruptive fissures (Fig. 3A) that may have controlled the
494 growth of the dome and stubby lava-flow complex. Available ages indicate a *c.*100 kyr-long
495 effusive activity for the Airport-Potrero dome cluster (Fig. 4).

496 *La Horqueta cumulo-dome*

497 La Horqueta (40 km², 3.24 – 6.46 km³) is a pile of superimposed domes with steep, overlapping,
498 stubby block-lava flows located in the central part of the younger edifice. Its lava flows extend
499 as far as 13 km southeast towards El Rodado and to the northwest it is covered by younger
500 flows of Nevado Chachani summit. The “lower unit” consists of andesite block-lava flows
501 (Hor1–Hor2). The middle unit, dated by U/Pb at 345 ± 26 ka, consists of andesite lava flows
502 (Hor3 and Hor4) that reached a ~6.3 km distance from the vent to the northwest. A pile of
503 andesite lava flows is found on the southeast side of the edifice as far as ~7 km from the summit.
504 One flow of the upper unit was U/Pb dated at 332 ± 29 ka.

505 *El Rodado stratocone*

506 Flows from the El Rodado (50 km², 6.26 – 9.17 km³) edifice overly the La Horqueta cumulo-
507 dome on its western flank. The lower unit is formed by andesite lava flows (Rod1 and Rod2).
508 Distally they cover older weathered volcanoclastic deposits that mantle the AAI on the upper
509 slopes of the basin. The middle unit consists of porphyritic andesite lava flows (Rod3–Rod5),
510 one of which was U-Pb dated at 239 ± 25 ka. The upper unit of El Rodado, which was emplaced
511 on the collapsed side of the middle unit, consists of andesite lava flows (Rod6 and Rod7). The
512 eruptive activity of the upper unit followed the Late Pleistocene collapse of the southern flank
513 of the middle unit, which left a 1.2 km-wide amphitheater open to the south.

514 *The Uyupampa compound lava-flow field*

515 A thick (~100 m) and stubby, compound aa and blocky lava-flow field (Uyu1 to Uyu3) of 16
516 km² and 2.36 – 2.72 km³ form the westernmost edge of the Chachani cluster. This andesitic,
517 compound field of blocky lava flows cover the lava flows of the El Rodado stratocone. The
518 second lava-flow field unit has an ⁴⁰Ar/³⁹Ar age of 232 ± 36 ka. While the El Rodado edifice is
519 morphologically older than the Uyupampa flows, their ages overlap within error. This indicates
520 that their activity was closely related in time.

521 *The Nevado Chachani stratocone*

522 Nevado Chachani summit edifice (45 km², 30.34–33.20 km³) forms the most recent and highest
523 stratovolcano of the C-LVC, towering at 6057 m asl. It consists of three units that were
524 emplaced in the central part of the Young Edifice group. The lower unit is located on the eastern
525 side of the summit complex, overlying El Angel stratovolcano (Cha1–Cha5). Block-lava flows
526 from the middle unit (Cha6 –Cha8) that cover the deposits of the La Horqueta cumulo-dome
527 were dated by U/Pb at 222 ± 24 ka and 202 ± 32 ka. A small, flattish andesite lava dome named
528 La Torta (Fig. 3A), probably emplaced under subglacial conditions as it displays glassy,
529 prismatic lava flow edges, is considered as part of this unit. The upper unit, emplaced over the
530 collapsed side of the lower unit, consists of andesite and dacite lava flows that have yielded
531 young ⁴⁰Ar/³⁹Ar ages of 131 ± 4 ka and 130 ± 38 ka. At the apex of the lava flows, which were
532 weathered beneath the former summit Ice cap, we observe four youthful craters.

533 *Cabrería dome-coulees*

534 These units consist of lava domes (Cab) and aprons of thick block-and-ash flow deposits, one
535 of these deposits being dated by ⁴⁰Ar/³⁹Ar at 56 ± 31 ka. The widespread (> 21 km², 4.13 – 4.91
536 km³) pyroclastic apron up to 9 km down towards the Arequipa airport and the town of Cayma

537 represents one of the most recent pyroclastic deposits from dome collapse events on the south
538 flank of Nevado Chachani.

539 *El Volcancillo dome*

540 A small ($\sim 1.2 \text{ km}^2$, $0.33\text{--}0.39 \text{ km}^3$) dacite lava-dome and a small lava flow (Vol) were emplaced
541 in a large glacial scar open to the west near the summit of Chingana stratovolcano. Its location
542 and lack of glacial erosion despite its elevation ($\sim 5200 \text{ masl}$) suggest that this is the most recent
543 (Late-Glacial times?) center of the C-LVC. Various attempts at $^{40}\text{Ar}/^{39}\text{Ar}$ -dating this lava dome
544 have, however, failed due to its young age and excess argon. However, based on morphological
545 observation, we propose to include the El Volcancillo dome into the Young Edifice group.

546 *5.2.3 Evidence for a stratigraphic gap*

547 During fieldwork, mapping, and sampling, we have not found other C-LVC deposit overlying the dated
548 *c.* 641 ka unit of El Colorado dome (the youngest of the Old Edifice group). In addition, one of the
549 lowermost units of El Angel edifice dated at *c.* 463 ka (i.e., the oldest of the Young Edifice group)
550 directly overlies the Chingana edifice. Thus, a distinct magmatic gap from *c.* 641 to 463 ka (Fig. 4) is
551 documented between the Old Edifice group (*c.* 1280 and 640 ka) and the Young Edifice group (*c.* 460 –
552 *c.* 56 ka).

553 **5.3 Late Pleistocene pyroclastic sequences of C-LVC**

554 Late Pleistocene pyroclastic deposits are almost absent on the upper flanks of C-LVC and were
555 probably covered by subsequent lavas and/or removed by glacier ice and meltwater above 3800
556 m asl. However, tephra-fall and PDC deposits, found on the lower flanks of the Old Edifice
557 group, for example on the north flank of Nocarane (beneath El Colorado dome), on the south
558 flank of the Estribo and lower east flank of Chingana edifices, are related to explosive activity.
559 Scoria flows including glassy breadcrust bombs indicating phreatomagmatic or subglacial
560 activity crop out on the western flank of the Nocarane edifice. The source is probably a scoria
561 cone located at 5.5 km distance at 4700 m ($16^{\circ}07'19.95\text{S}$, $71^{\circ}34'05.21\text{W}$).

562 More extensive and thicker pumice-rich lapilli fall layers are intercalated in El Misti PDC and
563 tephra successions on the SW and south flanks of Nevado Chachani, as well as in outcrops
564 towards the city of Arequipa (Independencia and Quebrada Pastores, Fig. 4). The 4 to 7 m-thick
565 pumice-fall sequence with distinct greenish color, scoriaceous texture, and mafic andesite
566 composition crops out between the 70-ka lava flow observed in the Quebrada Pastores valley
567 and the *c.* 46 ka 'Misti 2.2' PDC sequence (Thouret et al., 2001).

568 In the Young Edifice group, block-and-ash flow deposits are related to the Airport-Potrero and
569 the Cabreria domes (56 ± 31 ka, [Table 2](#)) on the lower south flank of the C-LVC.

570 Major Holocene activity at the Nevado Chachani volcanic cluster cannot be ruled out, although
571 no tephra depositor lava flows of that age have been identified so far. However, four breached
572 and unglaciated craters are preserved on the stratocone summit, and two vents adorn the eroded
573 summit ridge of the El Angel composite cone. These small summit craters could well be related
574 only to minor phreatic eruptions. Given the relatively young ages and extended periods of
575 activity and quiescence in the geological past, the southern Young Edifice group, in particular
576 the Nevado Chachani and El Angel stratocones should be considered presently dormant and
577 eruptions in the geological future should be expected.

578

579 **6. SUMMARY OF PETROGRAPHY AND MINERALOGY**

580 Modal analyses of the sample dataset are given in [Table 5](#). Modal analyses of the analysed
581 samples are given in [Table 5](#). We refer the readers to [ESD Petrography and Mineralogy, Table](#)
582 [2](#) and [ESD Figures 1-5](#) for further petrographic and mineralogical descriptions of the C-LVC
583 lava flows. Lavas of the Old Edifice group contain 6-38 vol.% phenocrysts (>500 μm) and
584 micro-phenocrysts (100-500 μm), and 62-94 vol.% groundmass (glass and microlites). The
585 most common phenocrysts and micro-phenocrysts include plagioclase (5-31 vol.%), amphibole
586 (1-8 vol.%), and ortho- and clinopyroxene (<7 vol.%), with olivine and biotite as accessory
587 minerals ([Fig. 7](#)), and rhyolitic glass (68-77 wt.% SiO_2).

588 The Young Edifice samples contain 13-45 vol.% phenocrysts and micro-phenocrysts, and 55-
589 87 vol.% groundmass. The dominant phenocrysts and micro-phenocrysts are plagioclase (11-
590 35 vol.%), amphibole (1-10 vol.%), ortho- and clinopyroxene (<5 vol.%), biotite is accessory
591 mineral, while olivine micro-phenocrysts are present only in lavas from La Torta dome ([Fig.](#)
592 [7](#)). The groundmass of andesites and dacites is comprised of plagioclase, amphibole, pyroxene,
593 and rhyolitic glass (73-78 wt.% SiO_2). As a whole, the mineral assemblage and the mineral
594 chemistry remain the similar during the entire C-LVC evolution (see [ESD Table 2](#)). However,
595 we observed a few differences; for instance, the fact that amphibole and biotite tend to be more
596 abundant in the felsic lavas, whereas olivine only appears in one basaltic andesite lava. In
597 addition, a few minerals (i.e., plagioclase and amphibole) display different textural types that
598 include euhedral, non-altered phenocrysts together with phenocrysts, showing frequent
599 disequilibrium textures such as spongy cellular (sieve) textures with cores, and concentric

600 growth zones and/or dissolution zones as well as late overgrowth rims in plagioclase. We also
601 note different types of amphibole breakdown textures, the fine-grained opaque rims from
602 dehydration that form during fast decompression and eruption and the coarse-grained
603 breakdown zones indicative of slower ascent (Rutherford and Hill, 1993). Both types of
604 disequilibrium textures are more frequent in the Young Edifice compared to the Old Edifice
605 group.

606

607 **7. TEMPORAL WHOLE-ROCK COMPOSITIONAL VARIATIONS**

608 **7.1. Evolution of major elements through the C-LVC lifetime**

609 Chemical data of bulk rock composition indicate three different patterns through time (Figs. 8
610 and 9, ESD Table 3): (1) the oldest Pre-Chachani lava units (>1.28 Ma) which crop out at the
611 Quebrada La Paccha show homogeneous lava compositions (mean = 60.12 wt.% SiO₂, SD=
612 0.10, N= 5). (2) The Old Edifice lavas (~1.00–0.64 Ma) display a wide range in silica content
613 (mean= 60.88 wt.% SiO₂, SD= 2.88, N= 62), whereas (3) the Young Edifice group lavas (0.46–
614 0.05 Ma) again show a narrow compositional range (mean= 61.54 wt.% SiO₂, SD= 1.44, N=
615 39). In the following descriptions, we will focus on both C-LVC lava groups, while we will not
616 describe the Pre-Chachani lavas.

617 **7.1.1. Compositional variations throughout the Old Edifice group**

618 Whole rock compositions (Figs. 8, 9) within the Old Edifice group change from andesite in the
619 “Upper Base Chachani” (~1.1 Ma) to basaltic andesite in the Upper Chingana stratovolcano
620 (~0.91 Ma). Composition from the Estribo stratovolcano changes along a narrow but reverse
621 trend with a swift variation from dacite (Lower Estribo unit) to andesite (Middle Estribo unit).
622 The third edifice (Upper Estribo ~0.81 Ma) follows a common differentiation trend from
623 andesite (59 wt.% SiO₂) to dacite (64 wt.% SiO₂), but the most recent Estribo lavas (~0.69 Ma)
624 exhibit a decrease in SiO₂ content (~62 wt.%). Lavas from Nocarane starts with dacite
625 compositions (66 wt.% SiO₂), and then show a trend from dacite to basaltic andesite and again
626 to dacite in the same unit (Lower Nocarane ~0.75 Ma). From Middle to Upper Nocarane, the
627 composition changes reversely to ~60 wt.% as does El Colorado dome (~58 wt.%).

628 **7.1.2. Compositional variations throughout the Young Edifice group**

629 The Young Edifice group display a smaller range in compositions (59–64 wt.% SiO₂; Figs. 8,
630 9) compared to the Old Edifice lavas. Lavas of El Angel composite volcano, that represent the

631 older flows of the Young Edifice group, display andesitic compositions (62-63 wt.% SiO₂). In
632 contrast, the peripheral Airport-Potrero Domes shows a wider compositional range from
633 andesites to dacites (59-64 wt.% SiO₂). Then, La Horqueta lava domes and El Rodado cone
634 show compositions limited to a relatively narrow andesite range (60–63 wt.% SiO₂). The central
635 Chachani composite volcano starts with slightly evolved dacites, but lavas change to andesites
636 with a decrease in SiO₂. Finally, the most recent eruptive activity of the C-LVC from the
637 Cabrería and Volcancillo domes again produced slightly more evolved lavas (62–64 wt.%
638 SiO₂).

639 **7.2. Trace element patterns through C-LVC lifetime**

640 A few trace elements (e.g., Ni, Cr, V, Sc, Sr and Eu; [ESD Fig. 7](#)) are negatively correlated with
641 SiO₂ contents, although scattering is observed in Ni, Sr and Cr. In lavas of the entire C-LVC,
642 chromium and nickel contents are low (< 90 and < 60 ppm, respectively). Only the less
643 differentiated basaltic andesite samples exceed these values in the Chingana and Nocarane
644 edifices. Large-ion-lithophile elements (LILE; e.g., Cs, Rb, K, Ba) are positively correlated
645 with SiO₂, except Sr, which displays a negative correlation, and Eu content that remains
646 constant throughout differentiation (not shown). Th and U display a moderate positive
647 correlation with SiO₂, whereas high field strength elements (HFSE, e.g., Nb, Ta, Zr, Hf) and
648 light rare earth elements (LREE, e.g., La, Ce, Nd) exhibit a slightly positive correlation with
649 SiO₂ increase. Middle and high rare earth elements (MREE and HREE; Sm and Y) show no
650 variations with increase in silica contents.

651 Primordial Mantle-normalized spider diagrams of the C-LVC lavas ([Fig. 10](#)) exhibit strong
652 enrichment in LILE (Rb, Ba, K, Sr) compared to HFSE (Nb, Ta), a typical feature for
653 subduction-zone magmas, especially those of the CVZ (e.g., [Wilson, 1986](#)). Old Edifice lavas
654 display stronger enrichment and wider ranges in Rb, Ba, Th and U, slight enrichment in Sr and
655 Y, and stronger depletion in Cs, Nb and Ta ([Fig. 10](#)). Young Edifice of the C-LVC exhibit a
656 unique pattern: all of them are strongly depleted in Nb and Ta, but slightly enriched in La and
657 Sr. The trace element distribution patterns are more uniform in the Young Edifice lavas than
658 those of the Old Edifice group.

659 **7.3. Chemical correlation between the C-LVC and the AA Ignimbrite**

660 The C-LVC has buried the source (large nested vents or a single caldera) of the AAI
661 ([Paquereau-Lebti et al., 2006, 2008](#)) within only several 100 ka. A genetic link and an evolution

662 in a common magmatic system should therefore be considered by testing their potential
663 geochemical relations.

664 Major element oxides in Harker diagrams and plot of incompatible elements (Cs, Rb, K and
665 Ba) against silica content suggest that C-LVC, AAI and LJI magmas form a single
666 differentiation trend (Fig. 11). On the other hand, LJI is enriched in Rb and Cs (not shown) but
667 is depleted in Ba compared to AAI. Ratios of K, Rb and less incompatible elements like Dy,
668 Ta, Yb, Nb indicate that the C-LVC and AAI follow a similar trend; in contrast, LJI shows
669 dispersed values (Fig. 11). For instance, Rb/Sr vs. SiO₂ diagram shows that C-LVC lavas and
670 AAI fall in the same differentiation pattern, whereas LJI display higher Rb/Sr values for similar
671 silica contents. Incompatible-element ratios such as Ba vs Th and B/Th vs. Dy/Yb (Fig. 11)
672 exhibit overlapping fields with higher values in Ba/Th in C-LVC and AAI samples compared
673 with lower Ba/Th ratios in LJI samples.

674 The gap in silica content between C-LVC lavas and ignimbrite sheets (from 66 to 75 wt.% SiO₂)
675 indicates that the more silicic magmas represented by the ignimbrites are significantly more
676 evolved and are affected by the dominant fractional crystallization of plagioclase and K-
677 feldspar. We document this process through the increasing Rb/Sr and decreasing Ba for
678 comparable SiO₂ and Th, respectively (Fig. 11).

679 **8. DISCUSSION**

680 **8.1. C-LVC growth and volume estimate**

681 Cross sections depicted in Figure 5 A, B point to hypothetical deep structures inferred from
682 field observations in areas adjacent to the C-LVC west and east of the Western Cordillera. From
683 maximal and minimal elevations (highest and lowest contact points between C-LVC and
684 bedrock; Fig. 5 A and B) measured around all edifices, the basal slope of C-LVC, as observed
685 in the Yura valley to the west and in the Arequipa basin to the SW, dips > 4° towards West and
686 > 5° towards SW and SE. One handicap is the fact that the basal contact surface between the
687 edifices and the bedrock is known only on the edges of the complex (e.g., along the Río Chili
688 canyon). We used three techniques to calculate the volume of C-LVC: (1) a network of x,y,z
689 dots (sampled each 1 km) tracing the exposed contact on the geologic map was integrated on
690 Surfer® software to construct an assumed C-LVC basal surface with the kriging interpolation
691 method. We then determined the volumetric difference between the 30-m DEM of the current
692 surface topography and the calculated basal surface, obtaining a volume of 289 km³.
693 Intersection points between the profiles (Fig. 5) and calculated surface were also used to build

694 a 3D-block diagram (Fig. 6). With the same principle but using (2) interpolation of Triangular
695 Irregular Networks (TIN) obtained from 30-m DEM data, and reference inclined contact surface
696 between bedrock and C-LVC derived from exposed outcrops, we computed a volume of 346
697 km³ on ArcMap® software. In addition, (3) considering the volcanoclastic deposits in the
698 western wall of the Río Chili canyon (base of Estribo edifice) and inclined reference basal
699 surface, we obtained a volume as large as 390 km³ with the NETVOLC (Euillades et al., 2013)
700 and MORVOLC algorithms (Grosse et al., 2012). Thus, we consider the two first estimated
701 values, which are similar within ~60 km³ as more accurate than the results using NETVOLC
702 and MORVOLC algorithms which deviate significantly from each other (190 - 390 km³). Table
703 4 shows ~290 (289) – ~350 (346) km³ the volume estimates for each edifice as well as the
704 eruption rates calculated from the volumes and know ages for each stratigraphic interval.

705 *8.1.1. Limitations and uncertainties in computing edifice volumes*

706 Uncertainties in computing the edifice volumes stem from poorly constrained parameters and
707 intrinsic limitations: (1) Surface areas are taken from the geologic map (Fig. 4) and 3D-
708 diagrams based on the reconstructed DEM (Fig. 6), while contacts have been derived from
709 exposed outcrops. (2) The thickness of lava piles and domes can only be roughly measured
710 except for the Airport-Potrero dome-coulees cluster and recent lava-flow fields that can be
711 directly measured in the field. (3) The geometry of deep structures beneath the Old Edifice
712 group remains poorly constrained, but the staircase morphology of the SW flank of Western
713 Cordillera (Fig. 6B) and active fault scarps (Río Chili, Aguada Blanca, Fig. 3A) has helped
714 suggest the pre-Chachani palaeo-tropography (Fig. 5), which was used to calculate the volume
715 of the C-LVC. (4) Estimated from the DEM and 3D-diagram (Figs. 4, 6), at least one fifth of
716 the initial volume of the older edifices has been removed either by glaciers, rockslides and
717 debris avalanches (Karátson et al. 2012), as shown by scars open on the SW-facing flanks of
718 the Estribo, El Angel, Chingana and Nocarane stratovolcanoes. (5) The volume of pyroclastic
719 deposits is small compared to lava flows and domes across the C-LVC, due to prevailing
720 effusive and extrusive activity and/or easier erosion of pyroclastic deposits by glaciers. Moraine
721 deposits cover the entire complex above 3800–3900 m in elevation, but an unknown volume of
722 pyroclastic deposits has been removed from the cluster by the Río Chili canyon and SW
723 drainages. Reworked glacial debris and volcanoclastic deposits have been exported out of the
724 cluster to the SW and SE, as shown by volcanoclastic deposits exposed along the walls of the
725 Río Chili canyon, and to the south onto the surface of the ignimbrite infill of the basin of
726 Arequipa. We have computed the area of volcanoclastic deposits on the top of AAI (south ring

727 plain of C-LVC) to be $180 \pm 10 \text{ km}^2$. Assigning 20 m for the deposit thickness (varying between
728 10 and 50 m), we estimated the volume to be in the range of 3.40 to 3.80 km^3 . The volume of
729 > 50 m-thick volcanoclastic deposits exposed on both walls of the Rio Chili canyon is likely
730 larger. Combined with the volume of deposits onto the top ignimbrite filling the basin, this leads
731 us to estimate, despite the uncertainty in the initial volume (Table 4), that at least 15% of the
732 initial Old Edifice group was removed away.

733 The computed volume of *c.* $63\text{--}75 \text{ km}^3$ for Young Edifice magmatism represents 25 to 39 % of
734 the volume estimate of the C-LVC Old Edifice (Table 4). Young Edifice are volumetrically
735 similar to well preserved composite cones of the Middle–Late Pleistocene Frontal arc in south
736 Peru (e.g., Ubinas, Misti and Ampato) and is larger than the $\sim 37 \text{ km}^3$ volume of the
737 Aucanquilcha volcano in Chile that was also built over a period of $\sim 1 \text{ Ma}$ (Klemetti and
738 Grunder, 2007). Moreover, the estimated *c.* $290 - 350 \text{ km}^3$ volume of the C-LVC compares
739 well with volumes computed for large regional volcano clusters or fields. For example, the
740 volume of Mount Mazama massif (Oregon, USA) with a 450 ka-long eruptive history is
741 estimated to be $58\text{--}112 \text{ km}^3$ (Bacon and Lanphere, 2006), taking into account that C-LVC size
742 and lifetime are twofold to 2.5 times these numbers.

743 **8.2 Eruption rates**

744 Given the limitations in accurately estimating volumes of dated deposits at high spatial and
745 temporal resolution, we can only focus on average, bulk eruption rates for each of the two
746 edifice groups. The Old Edifice eruptive rate, $0.27\text{--}0.41 \text{ km}^3/\text{ka}$ over a 600 kyr period, is in the
747 same order of magnitude than the $0.26\text{--}0.31 \text{ km}^3/\text{ka}$ entire C-LVC rate averaged over the 1.27
748 My lifetime (Table 4). The Young Edifice group eruptive rate ($0.12\text{--}0.15 \text{ km}^3/\text{ka}$) is 2.5 times
749 lower than that of the Old Edifice group. This is not surprising as (1) Old Edifice group cones
750 (e.g., Nocarane) are twice to three times as large as the most voluminous edifice of the Young
751 Edifice group (e.g., Chachani) and have almost two times higher eruptive rates compared to the
752 Young Edifice group (e.g., Chachani). Since we did not consider glacial erosion on the older
753 edifices, this difference should even be larger. (2) Young edifices, mostly domes and lava fields,
754 have not formed stratovolcanoes, although the youngest Nevado Chachani stratocone is likely
755 the fastest-growing C-LVC composite cone (Table 4), and (3) together with smaller
756 uncertainties in growth duration for domes, dome clusters, and silica-rich, compound ‘aa’ lava
757 fields. We bear in mind that such average eruption rates are highly skewed by the age range
758 over which volumes are integrated: for example, eruption rates of $0.12\text{--}0.15 \text{ km}^3/\text{ka}$ over the
759 460 kyr-long term Young Edifice magmatism are twice as high as the 50-200 kyr-short term

760 Old Edifice magmatism (0.01-0.03 km³/ka). The short-term eruption rates of the largest C-LVC
761 edifices (0.35-0.70 km³/ka) resemble the average growth rate of active composite cones in
762 southern Peru (Thouret et al., 2001; Samaniego et al., 2016) are in accordance with the
763 estimated 0.37 km³/ka magma eruption rate averaged at the CVZ scale over the past 10 My
764 (Francis and Hawkesworth, 1994). This is comparable to the long-term Mt. Mazama field
765 eruption rate of 0.42 km³/ka, which stems from the total volume of 176 km³ magma output in
766 the region over the past 420 kyr (Bacon and Lanphere, 2006). As pointed out by Hildreth and
767 Lanphere (1994), stratovolcanoes commonly grow in “spurts” superimposed on relatively
768 steady and low long-term productivity. Here in C-LVC, only composite cones as recent as
769 Chachani show relatively high eruptive rates (0.27-0.31 km³/ka) that are comparable to
770 averaged eruptive rates of individual volcanoes, e.g., Ubinas and Sabancaya (Rivera et al., 2014,
771 2017; Samaniego et al., 2016) in Peru and Parinacota in North Chile (0.25-0.31 km³/ka, Hora
772 et al., 2007). The eruptive rate over the 112 kyr-long Misti 2-4 stratocone growth with a
773 preserved volume of 73-80 km³ has been averaged at 0.63 km³/ka (Thouret et al., 2001), but
774 the Young Edifice group eruption rate is similar to the 0.12 km³/ka eruptive activity of the
775 Ampato-Sabancaya compound volcano (Tables 1 and 3).

776 **8.3 Petrogenetic processes acting during the C-LVC lifetime**

777 **8.3.1 Processes in the deep crust**

778 Compositional changes in time and space have been studied in magmas of the Central Andes
779 (e.g., Mamani et al., 2010; Wörner et al., 2018) in order to determine the relationship between
780 chemical signatures (major and trace elements and isotopic data) and the thickening process of
781 the continental crust. Trace element ratios such as Sr/Y, La/Yb, Sm/Yb and Dy/Yb may indicate
782 the crustal setting where magmatic differentiation (fractional crystallization and/or crustal
783 contamination) occurred. In the Central Andes, maximum Sr/Y and Dy/Yb ratios are observed
784 in intermediate andesites and dacites (55-65 wt.% SiO₂) erupted during the last 5 Ma; even if
785 low values in these ratios can occur at any time (Wörner et al., 2018). However, all C-LVC
786 lavas (53-67 wt.% SiO₂) do not show such maximum or minimum trace element ratios as
787 observed in Quaternary lavas (<2 Ma) in the Central Andes. Sr/Y, Dy/Yb and Sm/Yb ratios in
788 C-LVC vary between 23–71, 1.8–2.8 and 2.2–8 respectively, and these are intermediate values
789 (Fig. 12), compared with the composition of volcanic rocks of similar Pleistocene-Holocene
790 age in the CVZ (Wörner et al., 2018). Such intermediate values argue against a strong garnet
791 signature for the C-LVC magmas. In summary, REE systematics clearly suggest the lower-
792 middle crust fractionation of garnet is probably a minor process during the evolution of C-LVC

793 magmas. Small differences in Dy/Yb vs. Sm/Yb ratios of individual volcanoes in the C-LVC
794 may reflect the compositional variability of the crust and the complexity of the structural setting
795 between the Old- and the Young Edifice groups.

796 **8.3.2 Fractional crystallization, magma mixing, and crustal contamination**

797 The compositional and mineralogical variations in C-LVC lavas through time (See ESD Figs.
798 2 and 3) can be interpreted as the evolution of the magmatic system controlled by fractional
799 crystallization, assimilation, and magma mixing. Additional processes such as cumulate
800 recycling and remelting may also need to be considered. This interpretation stems from the
801 depletion in compatible elements with increasing silica contents and rather scattered trends in
802 incompatible vs. compatible element diagrams (Fig. 13). The two contrasted patterns displayed
803 in Figures 9 and 13 oppose the Old- to the Young Edifice group lava samples, suggesting a
804 progressive change to the homogenization or maturation of the C-LVC magmatic system. Other
805 trace elements (e.g., Rb and Ni) display a similar behavior.

806 At the same time, an increase in the average phenocrysts content of lavas (< 35 vol.% to
807 generally > 40 vol.%) and a two-fold decrease in magma eruptive rates (from 0.21-0.34 to 0.07-
808 0.09 km³/ka: Table 4) is documented between the Old- to Young Edifice group. We interpret
809 this observation as an indication that magma residence times increased and (degassing-driven)
810 crystallization and crystal recycling from previous magmatic events increased, suggesting a link
811 between higher crystallinity and lower eruption rate.

812 Trace element ratios versus silica contents allow us to infer fractional crystallization. In Figure
813 12A the positive correlation between the Ba/Sr ratio and silica content indicates the
814 fractionation of plagioclase. On the other hand, Dy/Yb ratio decreases slightly with SiO₂
815 increase (17C), whereas Sr/Y and Sm/Yb ratios display quite scattered values (17B, D). These
816 trends suggest a role of amphibole fractionation during differentiation (Davidson et al., 2007).
817 Decreasing Cr and Ni suggest removal of ferromagnesian minerals such as olivine and pyroxene
818 during the early stages of differentiation. A limited number of samples in Old Edifice group
819 show higher Cr and Ni values than the majority of C-LVC samples, while such high values are
820 correlated with olivine phenocrysts observed in the less differentiated lavas. The negative
821 correlation between Sr and Sc with silica contents point to crystallization of plagioclase and
822 pyroxene during the entire C-LVC lifetime.

823 In order to test the role of fractional crystallization, in figure 13 we plot a compatible (Ni)
824 against an incompatible element (Rb). The large dispersion observed suggests that fractional

825 crystallization is insufficient to explain the scattering. In this diagram fractional crystallization
826 of ferromagnesian minerals display a curved trend with a strong decrease of Ni coupled with a
827 weak increase of Rb, for the early fractional crystallization stages, and then a strong increase
828 of Rb (coupled with almost no variation of Ni). Using the mineralogical composition of the
829 cumulate estimated for Ubina magmatic series (46–48% Pl + 38–44% Amph + 3–5% Cpx +
830 6% Mag + 1% Apt; [Samaniego et al., 2020](#)) and the partition coefficients compiled by [Rivera
831 et al. \(2017\)](#), we estimated a Rayleigh fractional crystallization model using $D_{Rb} = 0.05$ and $D_{Ni} =$
832 4.00 as bulk distribution coefficient values. The comparison of the C-LVC geochemical data;
833 and in a more general the whole CVZ magmas (gray dots and dotted field in [Fig. 13](#)) clearly
834 shows that although the C-LVC samples show a global decrease of Ni with Rb increase, these
835 data do not follow the theoretical fractional crystallization trend. In contrast, mixing process
836 between a primitive (with high Ni and low Rb contents) and a differentiated endmember (with
837 low Ni and high Rb contents) can explain the geochemical variability of C-LVC magmas. These
838 trends indicate complex magmatic processes involving fractional crystallization (coupled with
839 variable crustal assimilation) and frequent magma mixing. This is consistent with the trace
840 elements and isotopic lines of evidence that constrain the crustal contamination in Peruvian
841 volcanoes at around 10–20% at both regional ([Mamani et al., 2010](#); [Blum-Oeste and Wörner,
842 2016](#)) and local scales (Ubina, [Thouret et al., 2005](#); [Samaniego et al., 2020](#); Misti, [Rivera et
843 al., 2017](#); Ampato-Sabancaya, [Gerbe and Thouret, 2004](#); [Samaniego et al., 2016](#)).

844 **8.3.3. Disequilibrium textures as evidence for open system evolution**

845 ‘Sieve’ textures are related to rapid growth, whereas spongy cellular textures ([Fig. 7](#)) are
846 commonly attributed to pervasive dissolution (e.g., [Ruprecht and Wörner, 2007](#)). The sieve
847 textures can be interpreted as the result of magma mixing, but also from rapid decompression
848 with no substantial heat changes ([Nelson and Montana, 1992](#)). Breakdown textures appear
849 when an existing mineral is out of equilibrium and transforms into a new set of minerals instead
850 of dissolving ([Streck, 2008](#)). Such textures are observed in most of the C-LVC samples, where
851 the crystal edges are affected, producing reaction rims or generating pseudomorphs. Some
852 amphibole, biotite, orthopyroxene and olivine crystals show sub-rounded or rounded shapes
853 due to dissolution caused by resorption processes. In the C-LVC lava samples, breakdown
854 textures might be produced by pressure decrease and volatile lost during magma ascent.

855 In summary, the frequent disequilibrium textures observed in plagioclase phenocrysts as well
856 as the chemical variations of plagioclase and amphibole indicate that magma mixing/recharge
857 are prominent processes throughout the entire history of the C-LVC.

858 Based on plagioclase pheno- and microcrysts compositions (see ESD Fig. 2), we argue that
859 fractional crystallization alone would not explain the chemical diversity of C-LVC magmas.
860 We suggest that magma recharge and subsequent mixing or mingling processes also play an
861 important role during the C-LVC evolution. In this context, two non-exclusive models have
862 been proposed in the literature (Couch et al., 2001; Ruprecht and Wörner, 2007): (1) the
863 physical mixing between magmas of contrasting compositions, temperatures and physical
864 properties; and (2) the recharge of a magmatic reservoir by mafic magma, producing an increase
865 in temperature and thus thermal convection, without physical mixing between these magmas.
866 In order to discriminate between these processes, Ruprecht and Wörner (2007) proposed to
867 focus on the systematic variations of anorthite and Fe contents in plagioclase. Given that Fe is
868 a trace element in feldspars, only the melt composition and degree of oxidation may affect Fe
869 content in plagioclase (Ginibre et al., 2002; Ruprecht and Wörner, 2007). Based on this
870 assumption, observed increase in anorthite and Fe in plagioclase may be the result of physical
871 mixing process. In contrast, increase of anorthite values without variation in Fe may result from
872 thermal mixing (or “self-mixing”, Couch et al., 2001).

873 Taking the hypotheses based on increasing values in iron and calcium in reverse-zoned
874 plagioclase crystals, we suggest that many analyzed lava samples from Upper Chingana, Lower
875 Nocarane, Upper Estribo, La Torta, Upper Chachani and Volcancillo lavas were affected by
876 compositional mixing (Fig. 14). In contrast, the reverse and/or oscillatory zoning in plagioclase
877 crystals without iron increase in lava samples from El Rodado, La Horqueta, Airport-Potrero
878 Domes and Lower Chachani have recorded thermal mixing, probably due to thermal convection
879 in magma reservoirs.

880 As they have been observed in whole rock geochemistry, differences in plagioclase composition
881 between Old- and Young Edifice lavas are also remarkable. Old Edifice lavas show wider
882 ranges in An₃₀₋₈₀ and FeO (0.17–1.44 wt.%) values compared to Young Edifice group (An₂₉₋₆₇
883 and 0.15–0.72 wt.% FeO), with exception of La Torta dome (An₃₁₋₆₄ and 0.27–1.42 wt.% FeO),
884 which was emplaced to the north of La Horqueta cumulo dome. Differences in plagioclase and
885 amphibole composition (Fig. 14) might suggest that thermal and compositional mixing and
886 mafic recharge was more frequent processes in magmas emplaced during the Old Edifice group
887 as compared to the Young Edifice group.

888 **8.4 Implications of C-LVC on CVZ magmatic regimes and transcrustal magmatic systems** 889 **in southern Peru**

890 A model of transcrustal magma feeding systems for the CVZ has been proposed to define three
891 magmatic regimes controlled by the recharge of hotter and less evolved magmas that ascend
892 from depth into shallow reservoirs below arc volcanoes in the Central Andes (Wörner et al.,
893 2018, and Fig. 15). These three regimes are: (1) The accumulation regime (steady state) referred
894 to low recharge rates of the reservoirs over a few of millions of years producing uniform hybrid
895 dacites with slow growth of volcanoes. (2) The activation regime, which consists of increasing
896 mafic recharge that produce higher eruption rates with emission of a wide range of compositions
897 (basaltic andesites to rhyolites) during several hundreds of kyr. (3) The breakthrough regime
898 occurring with high recharge rates producing mafic to intermediate andesites and occurs in the
899 younger edifices during a time span of several kyr.

900 The C-LVC case study demonstrates that volcanic clusters can experience a shift between
901 steady and unsteady, accumulation and activation regimes. Petrographic differences such as the
902 increase in phenocryst content and maximum crystal size, decrease of An-contents in
903 plagioclase and Ca-content in pyroxene from Old- to Young Edifice group magmas indicate
904 important changes during the long and continuous evolution of C-LVC. The large
905 compositional range and relatively fast eruption rate during the early (> 0.6 Ma) cluster may
906 likely relate to higher rates of mafic recharge and higher contrast in endmember compositions
907 during magma mixing. The narrow compositional range (also observed in most incompatible
908 elements such as Rb, U, Th) and lowering of eruption rate towards the Young Edifice units (<
909 0.4 Ma) cluster suggests a process of “maturation” towards the younger (and more evolved)
910 magmatic stages. Changes back-and-forth between magmatic regimes depend on the rate of
911 mafic recharges from below and the size and temperature of resident, evolved magmas at
912 shallow levels. The zone of storage, mixing, differentiation and crystallization has not been
913 imaged in the upper crust below the C-LVC, but two independent lines of evidence stem from
914 recent studies that suggested the existence of evolved magmas at shallow depths <15 km.

915 1. A recent seismological study highlighted the existence of a strong scatter of seismic energy
916 coinciding with a low-velocity zone at a depth of 5–10 km “located at 71.6°W-16.1°S with an
917 error of 10 km beneath the dormant Nevado Chachani and the active El Misti” (Ma et al., 2013).
918 The authors modeled a vertical cylinder about 5 km in diameter that can be interpreted as a low-
919 velocity magma reservoir. This opens the possibility of repeated magma recharges from shallow
920 crustal depths compatible with recent thermo-barometric calculations on El Misti magmas
921 (Tepley et al., 2013; Rivera et al., 2017).

922 2. Mafic magma recharge and subsequent magma mixing under arc volcanoes around the C-
923 LVC have been suggested by studies of disequilibrium textures and mineral chemistry of
924 eruptive products recently erupted at Sabancaya (Gerbe and Thouret, 2004), Ubinas (Thouret
925 et al., 2005; Rivera et al., 2017; Samaniego et al., 2020) and Tutupaca (Manrique et al., 2020).
926 The depth of magma reservoirs has been estimated in the range of 9 to 15 km below the craters
927 of El Misti (Rivera et al., 2017) and Ubinas (Rivera et al., 2014; Samaniego et al., 2020); a
928 spherical-shape deformation source was identified at 11-14 km north of Sabancaya volcano
929 below the Hualca Hualca volcano during the ongoing eruptive period that started in November
930 2016 (Cruz, 2019). The temporal evolution towards more uniform and evolved composition,
931 and the petrology dataset (see section 7) support the hypothesis that the long-lived C-LVC
932 represents a long-lived and slowly evolving transcrustal magma system. The compositional
933 variety of magmas in the Old Edifice group suggests increased but variable recharges from
934 below into the shallow reservoir.

935 This thermally ‘alive’ upper crust may have prevailed further back since early Pleistocene time,
936 as the 1.28, 1.40, and 1.62–1.66 Ma ignimbrite eruptions point to the absence of any protracted
937 lull in the eruptive activity in the region in which the C-LVC has grown. Interesting questions
938 arise from the close temporal relation between the ignimbrite eruptions directly preceding the
939 onset of eruptions at the C-LVC. Intense eruptions of silicic magma are recorded by the Yura
940 Tuffs and the Arequipa Airport ignimbrite between 1.66 and 1.28 Ma, i.e., immediately before
941 the onset of magmatic activity at the Chachani cluster (<1.28 Ma). How are these magmatic
942 systems related? Is the C-LVC a dying magmatic system that followed a larger silicic magma
943 reservoir that fed the ignimbrites? Does the focus of magmatism change in depth with time? Or
944 is there a change from silicic magma ponding during the ignimbrite stage followed by:
945 increasing recharge rates that resulted in a “break-through” of mafic recharge magmas and
946 increased mixing and reactivation of older crystal-rich magmas in a mushy transcrustal
947 reservoir? These questions need to be addressed by further analytical work focusing in
948 particular on compositional variations and zonations on phenocryst minerals and diffusion
949 speedometry of magmatic processes.

950

951 **CONCLUDING REMARKS**

952 The evolution of the Chachani large volcanic cluster (C-LVC) reveals how these long-lived
953 volcanic structures grow from transcrustal magma systems in the CVZ and why magmatic

954 regimes have shifted from initial large compositional variations to steady state, monotonous
955 andesitic regime through the *c.* 1.28 Myr cluster lifetime.

956 1. Twelve volcanic edifices overlying the Pre-Chachani lavas (>1278 ka) have formed (i) the
957 Early to Middle Pleistocene Old Edifice group (<1100–640 ka) with a relatively large range
958 from basaltic andesite to dacite compositions (53–67 wt.% SiO₂), and (ii) the middle to late
959 Pleistocene group (>400–56 ka) of Young Edifice domes and dome-coulee complexes,
960 stratocones and lava flow fields showing a narrower range of andesitic and minor dacitic
961 compositions (58–64 wt.% SiO₂).

962 2. The volume of each of the C-LVC edifices has been estimated despite a number of
963 uncertainties. The DEM-based calculations yielded a 289 and 346 ± 29/35 km³ range. The Old
964 Edifice group represent two thirds of the C-LVC volume, whereas the Young Edifice volume
965 represents about the remaining one third of the estimated volume. Young edifices are
966 volumetrically similar to young, weakly eroded stratocones of the frontal arc in southern Peru.

967 3. Slow bulk eruption rates estimated for both groups of edifices are similar to comparable CVZ
968 long-lived clusters (e.g., Aucanquilcha, North Chile) or elsewhere (e.g., Mt. Mazama and Crater
969 Lake volcanic centres, Cascades). Eruptive rates have slowed down twofold from Old Edifice
970 (0.27–0.41 km³/ka) to Young Edifice C-LVC (0.12–0.15 km³/ka), coinciding with monotonous
971 andesitic compositions. This suggests that the C-LVC magmatic system became mature with
972 time. This means that slow but constant eruptive rates feeding Young Edifice magmatism
973 produced uniform, evolved compositions by continuous mafic recharge, magma mixing and
974 thermal stabilization. A similar, stable magmatic system with uniform erupted magma
975 compositions and evidence for long-lasting temperature cycling of the magma reservoir was
976 documented for the dacitic Taápaca volcano in North Chile ([Rout and Wörner, 2021](#)).

977 4. Bulk rock major and trace elements highlight the fact that C-LVC compositions have varied
978 along three different periods: following homogeneous compositional range of the Pre-Chachani
979 and Chachani base lava flows, the range expands in lavas of the Old Edifice group, but the
980 compositions narrowed and became relatively homogeneous in the Young Edifice lavas. This
981 suggests changes in magma source location and/or repeated magma recharge and thermal
982 pulses.

983 5. Bulk rock and mineral chemical analyses suggest that the C-LVC represents protracted post-
984 caldera activity, which directly followed the 1.62–1.66 Ma Arequipa Airport ignimbrite. This
985 confirms the genetic link between this medium-sized ignimbrite event and the subsequent

986 evolution of the C-LVC thus significantly expanding the lifetime and volume of this magmatic
987 system.

988 6. Mineral disequilibrium textures and composition changes support frequent recharge events
989 during the C-LVC lifetime. FeO–An systematics used in plagioclase crystals indicate
990 compositional mixing or mingling in samples of the late events during Old- and in the Young
991 Edifice magmatism.

992

993 **Acknowledgments**

994 We thank the Editor, K. Russell, and reviewers E. Klemetti and D. Karátson for their comments
995 and constructive suggestions made on the early version of the manuscript, which helped to
996 improve its content. This work stems from the first author's Master study hosted at the
997 Laboratoire Magmas et Volcans in Clermont-Ferrand with the support of the French Centre
998 National de Recherche Scientifique and Institut de Recherche pour le Développement. The
999 initial internship work was supported by the Réseau inter-universitaire R. Porras Barrenechea
1000 of the French Embassy in Peru. Part of the sampling and analytical work of G.W. was supported
1001 by the German Science Foundation grant Wo362/31-1. We thank late H. Martin, V. Carlotto
1002 and INGEMMET for administrative support in France and Peru, M. Benbakkar for ICP-AES
1003 analyses, J.L. Devidal for microprobe analyses, P. Grosse for helping us using the MORVOLC
1004 software, E. Romero for field assistance, and the LMV technical staff in particular C.
1005 Fonquernie for continuous support in laboratory analyses.

1006

1007 **References**

- 1008 [Aguilar, R.](#), 2015. Long-lived magmatic systems: the post-caldera Chachani volcanic complex
1009 case study, Peru. MSc report (Unpubl.), Laboratoire Magmas et Volcans, Université
1010 Clermont-Auvergne, Clermont-Ferrand
- 1011 [Armijo, R.](#), [Lacassin, R.](#), [Coudurier-Curveur, A.](#), [Carrizo, D.](#), 2015. Coupled tectonic
1012 evolution of Andean orogeny and global climate. *Earth-Sci Rev* 143: 1–35
- 1013 [Bacon, C.](#), [Lanphere, M.](#), 2006. Eruptive history and geochronology of Mount Mazama and
1014 the Crater Lake region. *Geol Soc Amer Bull* 118(11/12): 1331-1359

- 1015 Benavente, C., Delgado, F., García, B., Aguirre, E., Audin, L., 2017. Neotectónica, Evolución
1016 y Peligro Sísmico en la Región Arequipa. INGEMMET, Boletín Serie C: Geodinámica e
1017 Ingeniería Geológica N° 64, 395 pp
- 1018 Benavides-Cáceres, V., 1999. The Andean cycle. In: Skinner BJ (ed.), *Geology and ore*
1019 *deposits of the Central Andes*. Soc Eco Geol Spec Publ 7: 61-107
- 1020 Bernard. K., Thouret, J.-C., Van Wyk de Vries, B., 2017. Emplacement and transformations
1021 of volcanic debris avalanches – A case study at El Misti volcano, Peru. *J Volcanol Geotherm*
1022 *Res* 340: 68-91
- 1023 Blum-Oeste, M., Wörner, G., 2016. Central Andean magmatism can be constrained by three
1024 ubiquitous end-members. *Terra Nova*: 1-7, doi: 10.1111/ter.12237
- 1025 Bromley, G., Thouret, J-C, Schimmelpfennig, I., Mariño, J., Valdivia, D., Rademaker, T.,
1026 Vivanco Lopez SdP., ASTER Team, Aumaître, G., Bourlès, D., Keddadouche, K., 2019. In
1027 situ cosmo-genic ^3He and ^{36}Cl and radiocarbon dating of volcanic deposits refine the
1028 Pleistocene and Holocene eruption chronology of SW Peru. *Bull Volc* 81: 64
- 1029 Carlotto, V., Quispe, J., Acosta, H., Rodríguez, R., Romero, D., Cerpa, L., Mamani, M., Díaz-
1030 Martínez, E., Navarro, P., Jaimes, F., Velarde, T., Lu, S., Cueva, E., 2009. Dominios
1031 geotectónicos y metalogénesis del Perú. *Bol Soc Geol Perú* 103: 1-89
- 1032 Clavero, J.E., Sparks, R.S.J., Pringle, M.S., Polanco, E., Gardeweg, M.C., 2004. Evolution and
1033 volcanic hazards of Taápaca Volcanic Complex, Central Andes of Northern Chile. *J Geol Soc*
1034 *London* 161: 603-618, doi.org/10.1144/0016-764902-065
- 1035 Coombs, M.L., Jicha, B.R., 2021. The eruptive history, magmatic evolution, and influence of
1036 glacial ice at long-lived Akutan volcano, eastern Aleutian Islands, Alaska, USA. *Geol Soc*
1037 *Amer Bull* 133 (5-6): 963–991
- 1038 Couch, S., Sparks, R.S.J., Carroll, M.R., 2001. Mineral disequilibrium in lavas explained by
1039 convective self-mixing in open magma chambers. *Nature* 411: 1037–1039
- 1040 Cruz, L., 2019. Análisis de deformación del volcán Sabancaya como herramienta útil en el
1041 pronóstico de erupciones periodo 2012–2017. Tesis de grado Universidad Nacional San
1042 Agustín, Arequipa
- 1043 Davidson, J.P., Turner, S., Handley, H., Macpherson, C., Dosseto, A., 2007. Amphibole
1044 “sponge” in arc crust? *Geology* 35(9): 787, doi:10.1130/g23637a.1

- 1045 [Davidson, J.P., McMillan, N.J.M., Moorbath, S., Wörner, G., Harmon, R.S., Lopez-Escobar,](#)
1046 [L.,](#) 1990. The Nevados de Payachata volcanic region (18°S/69°W, N Chile). II. Evidence for
1047 widespread crustal involvement in Andean magmatism. *Contrib Mineral Petrol* 105: 412-432.
- 1048 [Davidson, J.P., Harmon, R.S., Wörner, G.,](#) 1991. The source of Central Andean magmas; some
1049 considerations. In: Harmon RS, Rapela CW (eds) *Andean Magmatism and its tectonic setting.*
1050 *Geol Soc Amer Spec Paper* 265: 233-244
- 1051 [Delacour, A., Gerbe, M.-C., Thouret, J.-C., Wörner, G., Paquereau, P.,](#) 2007. Magma evolution
1052 of Quaternary minor volcanic centres in Southern Peru, Central Andes. *Bull Volc* 69, 6: 581-
1053 606
- 1054 [de Silva, S.L., Kay, S.M.](#) (2018) Turning up the heat: High-flux magmatism in the Central
1055 Andes. *Elements* 14: 245-250. DOI: 10.2138/gselements.14.4.245
- 1056 [Feeley, T.C., Davidson, J.P., Armendia, A.,](#) 1993. The volcanic and magmatic evolution of
1057 Volcan Ollaguë, a high-K, late Quaternary stratovolcano in the Andean Central Volcanic
1058 Zone. *J Volc Geoth Res* 54: 221-245
- 1059 [Feeley, T.C., Davidson, J.P.,](#) 1994. Petrology of calc-alkaline lavas at Volcán Ollaguë and the
1060 origin of compositional diversity at Central Andean stratovolcanoes. *J Petrol* 35: 1295–1340
- 1061 [Francis, P.W.,](#) 1993. *Volcanoes. A Planetary Perspective:* Oxford University Press, 443 pp
- 1062 [Francis PW, Hawksworth CJ](#) (1994) Late Cenozoic rates of magmatic activity in the Central
1063 Andes and their relationships to continental crust formation and thickening. *J Geol Soc*
1064 London 151: 845–854
- 1065 [Froger, J.L., Remy, D., Bonvalot, S., Legrand, D.,](#) 2007. Two scales of inflation at Lastarria-
1066 Cordon del Azufre volcanic complex, central Andes, revealed from ASAR-ENVISAT
1067 interferometric data. *Earth Planet Sci Lett* 255, 1-2: 148-163
- 1068 [Garcia, F., Chorowicz, J., Legros, F.,](#) 1997. La caldera Chachani, gran centro explosivo
1069 Plioceno-Holoceno del sur del Perú? Identificación y evolución en imagenes Landsat y Radar
1070 ERS. *Soc Geol Perú*, vol esp 1: 449-454
- 1071 [Gardeweg, M.C., Sparks, R.S.J., Matthews, S.J.,](#) 1998. Evolution of Lascar volcano, Northern
1072 Chile. *J Geol Soc London* 155: 89-104

- 1073 [Gerbe, M.C., Thouret, J.-C.](#), 2004. Role of magma mixing in the petrogenesis of lavas erupted
1074 through the 1990–98 explosive activity of Nevado Sabancaya in south Peru. *Bull Volcanol*
1075 66, 541–561
- 1076 [Ginibre, C., Kronz, A., Wörner, G.](#), 2002. High resolution quantitative imaging of plagioclase
1077 composition using accumulated back scattered electron images: new constraints on oscillatory
1078 zoning. *Contrib Mineral Petrol* 142: 436-448
- 1079 [Godoy, B., Wörner, G., Kojima, S., Aguilera, F., Simon, K., Hartmann, G.](#), 2014. Low pressure
1080 evolution of arc magmas in thickened crust: the San Pedro-Linzor volcanic chain, Central
1081 Andes, Northern Chile. *J South Amer Earth Sci* 52: 24-42
- 1082 [Gonzales, K., Finizola, A., Lénat, J.-F., Macedo, O., Ramos, D., Thouret, J.-C., Fournier, N.,
1083 Cruz, V., Pistre, K.](#), 2014. Asymmetrical structure, hydrothermal system and edifice stability:
1084 The case of Ubinas volcano, Peru, revealed by geophysical surveys. *J Volc Geoth Res* 276:
1085 132–144
- 1086 [Grosse, P., Euillades, P.A., Euillades, L.D., Van Wyk de Vries, B.](#), 2013. A global database of
1087 volcano morphometry. *Bull Volc* 76, 784 DOI 10.1007/s00445-013-0784-4
- 1088 [Grosse, P, van Wyk de Vries, B, Euillades, PA, Kervyn, M, Petrinovic, IA](#), 2012. Systematic
1089 morphometric characterization of volcanic edifices using digital elevation models.
1090 *Geomorphology*, 136: 114-131
- 1091 [Grosse, P., van Wyk de Vries, B., Petrinovic, I.A., Euillades, P.A., Alvarado, G.](#), 2009.
1092 Morphometry and evolution of arc volcanoes. *Geology* 37, 651–654.
- 1093 [Grunder, A.L., Klemetti, E.W., Feeley, T.C., McKee, C.M.](#), 2008. Eleven million years of arc
1094 volcanism at the Aucanquilcha Volcanic Cluster, Northern Chilean Andes: implications for
1095 the life span and emplacement of plutons. *Trans Royal Soc Edinburgh-Earth Sci* 97: 415-436
- 1096 [Guevara, C.](#), 1969. Geología del cuadrángulo de Characato. Servicio de Geología y Minería,
1097 Bol. 23, 53 p., color map 1: 100 000, Lima
- 1098 [Harpel, C., da Silva, S., Salas, G.](#), 2011. The 2-ka eruption of Misti volcano, southern Peru -
1099 The most recent plinian eruption of Arequipa's iconic volcano. *Geol Soc Amer Spec Paper*
1100 484: 1-72
- 1101 [Hildreth, W., Lanphere, M.A.](#), 1994. Postassium-Argon geochronology of a basalt-andesite-
1102 dacite arc system—The Mount Adams volcanic field, Cascade Range of Western
1103 Washington. *Geol Soc Amer Bull* 106: 1413-1429

- 1104 [Hildreth, W., Fierstein, J., Lanphere, M.A.](#), 2003. Eruptive history and geochronology of the
1105 Mount Baker volcanic field, Washington. *Geol Soc Am Bull* 115: 729–764
- 1106 [Hora, J.M., Singer, B., Wörner, G.](#), 2007. Volcano evolution and eruptive flux on the thick crust
1107 of the Andean Central Volcanic Zone: $^{40}\text{Ar}/^{39}\text{Ar}$ constraints from Volcán Parinacota, Chile.
1108 *Geol Soc Amer Bull* 119, 3/4: 343-362
- 1109 [Hoshizumi., H., Uto, K., Watanabe, K.](#), 1999. Geology and eruptive history of Unzen Volcano,
1110 Shimabara Peninsula, Kyushu, SW Japan. *J Volc Geoth Res* 89, 1–4: 81–94
- 1111 [Hurai, V., Paquette, J.L., Huraiová, M., Konecny, P.](#), 2010. Age of deep crustal magmatic
1112 chambers in the intra-Carpathian back-arc basin inferred from LA-ICPMS U-Th-Pb dating of
1113 zircon and monazite from igneous xenoliths in alkali basalts. *J Volc Geoth Res* 198:275-287
- 1114 [James, D.E.](#), 1982. A combined O, Sr, Nd and Pb isotopic and trace element study of crustal
1115 contamination in central Andean lavas. I: Local geochemical variations. *Earth and Planetary*
1116 *Science Letters*, 57: 47-62, doi.10.1016/0012-821X(82)90172-8
- 1117 [James, D.E., Sacks, I.S.](#), 1999. Cenozoic formation of the Central Andes: A geophysical
1118 perspective, *in* Skinner, B.J., ed., *Geology and Ore Deposits of the Central Andes*. Society of
1119 Economic Geologists Special Publication, 7: 1-25
- 1120 [Jenks, W.](#), 1948. Geología de la hoja de Arequipa a escala 200 000. Boletín 9, Carta Nacional,
1121 Lima, Peru
- 1122 [Jicha, B.R., Rhodes, J.M., Singer, B.S., Garcia, M.O.](#), 2012. $^{40}\text{Ar}/^{39}\text{Ar}$ geochronology of
1123 submarine Mauna Loa volcano, Hawaii. *J Geophys Res* 117: B09204,
1124 doi:10.1029/2012JB009373
- 1125 [Karátson, D., Telbisz T., Worner, G.](#), 2012. Erosion rates and erosion patterns of Neogene to
1126 Quaternary stratovolcanoes in the Western Cordillera of the Central Andes: An SRTM DEM
1127 based analysis. *Geomorph* 139-140: 122-135
- 1128 [Klemetti, E.K., Grunder, A.L.](#), 2007. Volcanic evolution of Volcán Aucanquilcha, a long-lived,
1129 monotonous dacite volcano in the Central Andes of Northern Chile. *Bull Volc* 70: 633-650.
1130 Doi 10.1007/s00445-007-0158-x
- 1131 [Kuiper, K.F., Deino, A., Hilgen, F.J., Krijgsman, W., Renne, P.R., Wijbrans, J.R.](#), 2008.
1132 Synchronizing Rock Clocks of Earth History. *Science* 320: 500-504
- 1133 [Ludwig, K.R.](#), 2001. Users' manual for Isoplot/Ex rev. 2.49. Berkeley geochronology centre,
1134 Special Publ 1a, 55

- 1135 [Ma, Y., Clayton, R.W., Tsai, V.C., Zhan, Z., 2013. Locating a scatterer in the active volcanic](#)
1136 [area of Southern Peru from ambient noise cross-correlation. *Geophys J Internat* 192\(3\): 1332–](#)
1137 [1341. doi:10.1093/gji/ggs103](#)
- 1138 [Mamani, M., Tassara, A., Wörner, G., 2008. Composition and structural control of crustal](#)
1139 [domains in the central Andes. *Geochem Geophys Geosys* 9: 1-13](#)
- 1140 [Mamani, M., Wörner, G., Semperé, T., 2010. Geochemical variation in igneous rocks of the](#)
1141 [Central Andean orocline \(13 °S to 18 °S\): tracing crustal thickening and magmas generation](#)
1142 [through time and space. *Geol Soc Amer Bull* 97: 241–254](#)
- 1143 [Manrique, N., Samaniego, P., Médard, E., Schiavi, F., Marino, J., Liorzou, C., 2020. Pre-](#)
1144 [eruptive magmatic processes associated with the historical \(218 ±14 a BP\) explosive eruption](#)
1145 [of Tutupaca volcano \(southern Peru\). *Bull Volc* 82:6, doi.org/10.1007/s00445-019-1335-4](#)
- 1146 [Mariño, J., Samaniego, P., Manrique, N., Valderrama, P., Roche, O., Van Wyk de Vries, B.,](#)
1147 [Guillou, H., Zerathe, S., Arias, C., Liorzou, C., 2021. The Tutupaca volcanic complex](#)
1148 [\(Southern Peru\): Eruptive chronology and successive destabilization of a dacitic dome](#)
1149 [complex. *J South Amer Earth Sci* 109, 103227, doi.org/10.1016/j.jsames.2021.103227](#)
- 1150 [Mariño, J., Thouret, J.C., Cabrera, M., Aguilar, R., Manrique, N., Edwards, B., Kochtitzky, W.,](#)
1151 [2020. Geología y evaluación de los peligros del complejo volcánico Nevado Coropuna.](#)
1152 [Boletín Geológico, INGEMMET, Lima: 145 pp](#)
- 1153 [Mathews, S.J., Jones, A.P., Gardeweg, M.C., 1994. Lascar volcano, northern Chile: evidence](#)
1154 [for steady-state disequilibrium. *J Petrol* 35: 401–432](#)
- 1155 [Mering, C., Huaman-Rodrigo, D., Chorowicz, J., Deffontaines, B., Guillande, R., 1996. New](#)
1156 [data on the geodynamics of southern Peru from computerized analysis of SPOT and SAR](#)
1157 [ERS-1 images. *Tectonophys* 259: 153–169](#)
- 1158 [Meyers, S.R., Siewert, S.E., Singer, B.S., Sageman, B.B., Condon, D.J., Obradovich, J.D.,](#)
1159 [Jicha, B.R., Sawyer, D.A., 2012. Intercalibration of radioisotopic and astrochronologic time](#)
1160 [scales for the Cenomanian–Turonian boundary interval, Western Interior Basin, USA.](#)
1161 [Geology 40: 7–10](#)
- 1162 [Min, K., Mundil, R., Renne, P.R., Ludwig, K.R., 2000. A test for systematic errors in ⁴⁰Ar/³⁹Ar](#)
1163 [geochronology through comparison with U/Pb analysis of a 1.1-Ga rhyolite. *Geochim.*](#)
1164 [Cosmochim. Acta 64: 73-98](#)

- 1165 [Muir, D.D., Barfod, D.N., Blundy, J.D., Rust, A.C., Sparks, R.S.J., Clarke, K.M., 2015.](#) The
1166 temporal record of magmatism at Cerro Uturuncu, Bolivian Altiplano. In: Carrichi L, Blundy
1167 JD (eds), Chemical, physical and temporal evolution of magmatic systems 422, 1, Geol Soc
1168 London Spec Publ: 57-82
- 1169 [Mullen, E., Paquette, J.L., Tepper, J.H., McCallum, I.S., 2018.](#) Temporal and spatial evolution
1170 of Northern Cascade Arc magmatism revealed by LA-ICP-MS U-Pb zircon dating. *Canad J*
1171 *Earth Sci* 55: 443-462, doi:10.1139/cjes-2017-0167
- 1172 [Naranjo, J.A., 1992.](#) Chemistry and petrological evolution of the Lastarria volcanic complex in
1173 the north Chilean Andes. *Geol Mag* 129: 723-740
- 1174 [Nelson, S.T., Montana, A., 1992.](#) Sieved textured plagioclase in volcanic rocks produced by
1175 rapid decompression. *Amer Mineral* 77: 1242-1249
- 1176 [O'Callaghan, L.J., Francis, P.W., 1986.](#) Volcanological and petrological evolution of San Pedro
1177 volcano, Provincia El Lao, North Chile. *J Geol Soc London* 143, 2: 275-286
- 1178 [Ownby, S., Delgado Granados, H., Lange, R.A., Hall, C.M., 2007.](#) Volcán Tancítaro,
1179 Michoacán, Mexico, $^{40}\text{Ar}/^{39}\text{Ar}$ constraints on its history of sector collapse. *J Volc Geoth Res*
1180 161: 1-14
- 1181 [Paquereau-Lebti, P., Thouret, J.-C., Wörner, G., Fornari, M., 2006.](#) Neogene and Quaternary
1182 ignimbrites in the area of Arequipa, Southern Peru: Stratigraphical and petrological
1183 correlations. *J Volc Geoth Res* 154: 251-275, Doi 10.1016/j.jvolgeores.2006.02.014
- 1184 [Paquereau-Lebti, P., Fornari, M., Roperch, P., Thouret, J.-C., Macedo, O., 2008.](#)
1185 Paleomagnetic, magnetic fabric properties, and $^{40}\text{Ar}/^{39}\text{Ar}$ dating, of Neogene - Quaternary
1186 ignimbrites in the Arequipa area, Southern Peru. Flow directions and implications for the
1187 emplacement mechanisms. *Bull Volc* 70: 977-997
- 1188 [Paquette, J.L., Piro, J.L., Devidal, J.L., Bosse, V., Didier, A., Sannac, S., Abdelnour, Y., 2014.](#)
1189 Sensitivity enhancement in LA-ICP-MS by N₂ addition to carrier gas: Application to
1190 radiometric dating of U-Th-bearing minerals. *Agilent ICP-MS J* 58, 4-5
- 1191 [Peccerillo, A., Taylor, S.R., 1976.](#) Geochemistry of Eocene calc-alkaline volcanic rocks from
1192 the Kastamonu area, northern Turkey. *Contrib Mineral Petrol* 58: 63-81
- 1193 [Ramos, V., 2008.](#) The basement of the Central Andes: The Arequipa and related terranes. *Ann*
1194 *Rev Earth Planet Sci* 36, 289-324

- 1195 [Ramos, V.](#), 2010. The tectonic regime along the Andes: present-day and Mesozoic regimes.
1196 *Geol J* 45, 1: 2–25, doi.org/10.1002/gj.1193
- 1197 [Richards, J.P.](#), [Villeneuve, M.](#), 2001. The Lullailaco volcano, Northwest Argentina:
1198 construction by Pleistocene volcanism and destruction by sector collapse. *J Volc Geoth Res*
1199 105: 77–105
- 1200 [Rivera, M.](#), [Thouret, J.-C.](#), [Samaniego, P.](#), 2014. The 2006-2008 eruptive products of Ubinas
1201 volcano, Peru: characteristics and implications on eruptive dynamics, magma production and
1202 hazards. *J Volc Geoth Res* 270: 122-141
- 1203 [Rivera, M.](#), [Martin, H.](#), [Le Pennec, J.-L.](#), [Thouret, J.-C.](#), 2017. Petro-geochemical constraints
1204 on the source and evolution of magmas at El Misti volcano (Peru). *Lithos* 268-271: 240-259
- 1205 [Robin, C.](#), [Samaniego, P.](#), [Le Pennec, J.-L.](#), [Fornari, M.](#), [Mothes, P.](#), [van der Plicht, J.](#), 2010.
1206 New radiometric and petrological constraints on the evolution of the Pichincha volcanic
1207 complex (Ecuador). *Bull Volc* 72: 1109–1129, doi.org/10.1007/s00445-010-0389-0
- 1208 [Rout, S.S.](#), [Wörner, G.](#), 2021. Long-term temperature cycling in a shallow magma reservoir:
1209 insights from sanidine megacrysts at Taápaca volcano, Central Andes. *J Petrol*, egab010,
1210 doi.org/10.109.3/petrology/egab010
- 1211 [Ruprecht, P.](#), [Wörner, G.](#), 2007. Variable regimes in magma systems documented in plagioclase
1212 zoning patterns: El Misti strato-volcano and Andahua monogenetic cones. *J Volc Geoth Res*
1213 165: 142–162
- 1214 [Rutherford, M.J.](#), [Hill, P.](#), 1993. Magma ascent rates from amphibole breakdown: an
1215 experimental study applied to the 1980–1986 Mount St. Helens eruptions. *J Geoph Res*
1216 98:19667–19685, doi: 10.1029/93JB01613
- 1217 [Samaniego, P.](#), [Rivera, M.](#), [Manrique, N.](#), [Schiavi, F.](#), [Nauret, F.](#), et al., 2020. Linking magmatic
1218 processes and magma chemistry during the post-glacial to recent explosive eruptions of
1219 Ubinas volcano (southern Peru). *J Volc Geoth Res* 407: 107095,
1220 doi.org/10.1016/j.jvolgeores.2020.107095
- 1221 [Samaniego, P.](#), [Robin, C.](#), [Chazot, G.](#), [Bourdon, E.](#), [Cotton, J.](#), 2010. Evolving metasomatic
1222 agent in the Northern Andean subduction zone, deduced from magma composition of the long-
1223 lived Pichincha volcanic complex (Ecuador). *Contrib Mineral Petrol* 160:239-260, doi:
1224 10.1007/s00410-009-0475-5

- 1225 [Samaniego, P., Rivera, M., Mariño, J., Guillou, H., Liorzou, C., Zerathe, S., Delgado, R.,](#)
1226 [Valderrama, P., Scao, V.](#), 2016. The eruptive chronology of the Ampato-Sabancaya volcanic
1227 complex (southern Peru). *J Volc Geoth Res* 323: 110–128
- 1228 [Schärer, U.](#), 1984. The effect of initial ^{230}Th disequilibrium on young U-Pb ages: the Makalu
1229 case, Himalaya. *Earth Planet. Sci. Lett.* 67(2): 191–204, doi:10.1016/0012-821X(84)90114-6
- 1230 [Sempere, T., Jacay, J.](#), 2006. Estructura tectónica del Sur del Perú (Antearco, arco y Altiplano
1231 suroccidental). XIII Congreso Peruano de Geología, Extended Abstracts, Lima: 324-327
- 1232 [Sempere, T., Noury, M., Garcia, F., Bernet, M.](#), 2014. Elementos para una actualización de la
1233 estratigrafía del Grupo Moquegua, sur del Perú. In: XVII Congreso Peruano de Geología,
1234 Lima, Extended Abstracts, digital file “Sempere, T”, Soc Geol Perú, Lima
- 1235 [Singer, B.S., Thompson, R.A., Dungan, M.A., Feeley, T.C., Nelson, S.T., Pickens, J.C., Brown,](#)
1236 [L.L., Wulff, A.W., Davidson, J.P., Metzger, J.](#), 1997. Volcanism and erosion during the past
1237 930 k.y. at the Tatara-San Pedro complex, Chilean Andes 36° S. *Geol Soc Amer Bull* 109:
1238 127-142
- 1239 [Sparks, R.S.J., Folkes, C.B., Humphreys, M.C.S., Barfod, D.N., Clavero, J., Sunagua, M.C.,](#)
1240 [McNutt, S.R., Pritchard, M.E.](#), 2008. Uturuncu volcano, Bolivia: Volcanic unrest due to
1241 midcrustal magma intrusion. *Am J Sci* 308, 6: 727-769
- 1242 [Stern, C.R.](#), 2004. Active Andean volcanism: its geologic and tectonic setting. *Rev Geol Chile*
1243 31, 2: 161-206
- 1244 [Streck, M.J.](#), 2008. Mineral textures and zoning as evidence for open system processes. *Rev in*
1245 *Mineral* 69, 595–622
- 1246 [Suaña, E.](#), 2011. Estudio Geológico del Complejo Volcánico Chachani, Arequipa-Perú. Tesis
1247 de grado. Universidad Nacional San Agustín, Arequipa, 302 pp
- 1248 [Sun, S., McDonough, W.F.](#), 1989. Chemical and Isotopic Systematics of Oceanic Basalts:
1249 Implications for Mantle Composition and Processes. *Magmatism in the Ocean Basin. Geol*
1250 *Soc Amer Spec Paper* 42: 313–345
- 1251 [Tepley, F.J., de Silva, S., Salas, G.](#), 2013. Magma dynamics and petrological evolution
1252 leading to the VEI 5 2000 BP eruption of El Misti volcano, southern Peru. *J Pet* 54, 10: 2033–
1253 2065

- 1254 [Tera, F., Wasserburg, G.J., 1972. U–Th–Pb systematics in three Apollo 14 basalts and the](#)
1255 [problem of initial Pb in lunar rocks. Earth Planet. Sci. Lett. 14, 281–304](#)
- 1256 [Thorpe, R.S., Francis, P.W., Hammil, M., Baker, M.B., 1982. The Andes, In: Thorpe RS \(Ed.\),](#)
1257 [Andesites, pp. 187–205](#)
- 1258 [Thouret, J.-C., Finizola, A., Fornari, M., Legeley-Padovani, A., Suni, J., Frechen, M., 2001.](#)
1259 [Geology of El Misti volcano near the city of Arequipa, Peru. Geol Soc Amer Bull 113, 12:](#)
1260 [1593–1610](#)
- 1261 [Thouret, J.-C., Dávila, J., Juvigné, E., Gourgaud, A., Boivin, P., 2002. Reconstruction of the](#)
1262 [AD 1600 explosive eruption at Huaynaputina volcano, Peru, based on geologic evidence and](#)
1263 [Spanish chronicles. J Volc Geoth Res 115, 3-4: 529-570](#)
- 1264 [Thouret, J.-C., Rivera, M., Wörner, G., Gerbe, M.-C., Finizola, A., Fornari, M., Gonzales, K.,](#)
1265 [2005. Ubinas: evolution of the historically most active volcano in Southern Peru. Bull Volc](#)
1266 [67: 557-589](#)
- 1267 [Thouret, J.-C., Wörner, G., Singer, B., Gunnell, Y., Zhang, X., Souriot, T., 2007.](#)
1268 [Geochronologic and stratigraphic constraints on canyon incision and Miocene uplift of the](#)
1269 [Central Andes in Peru. Earth Planet Sci Lett 263:151-166](#)
- 1270 [Thouret, J.C., Mamani, M., Wörner, G., Paquereau-Lebti, P., Gerbe, M.-C., Delacour, A.,](#)
1271 [Juvigné, E., Rivera, M., Mariño, J., Cacya, L., Singer, B., 2008. Neogene ignimbrites and](#)
1272 [volcanic edifices in southern Peru: stratigraphy, time-volume-composition relationships, and](#)
1273 [recent tephra-chronology. 7th International Symposium Andean Geodynamics ISAG, 2-4](#)
1274 [September 2008, Nice, Extended Abstracts: 545-548](#)
- 1275 [Thouret, J.-C., Jicha, B., Paquette, J.-L., Cubukcu, E., 2016. A 25 Myr chronostratigraphy of](#)
1276 [ignimbrites in South Peru. Implications for the volcanic history of the Central Andes. J Geol](#)
1277 [Soc London 173: 734-756, doi: 10.1144/jgs2015-162](#)
- 1278 [Thouret, J.-C., Gunnell, Y., Jicha, B., Paquette, J.-L., Braucher, R., 2017. Canyon incision](#)
1279 [chronology based on ignimbrite stratigraphy and cut-and-fill sediment sequences in SW Peru](#)
1280 [documents intermittent uplift of the western Central Andes. Geomorph 298: 1-19](#)
- 1281 [Tosdal, R.M., Farrar, E., Clark, A.H., 1981. K-Ar geochronology of the late Cenozoic volcanic](#)
1282 [rocks of the Cordillera Occidental, southernmost Peru. J Volc Geoth Res 10: 157-173, doi:](#)
1283 [10.1016/0377-0273\(81\)90060-3](#)

- 1284 [Van Achterbergh, E., Ryan, C.G., Jackson, S.E., Griffin, W.L.](#), 2001. Data reduction software
1285 for LA-ICP-MS (appendix), In : Sylvester PJ (ed.), Laser Ablation –ICP-Mass Spectrometry
1286 in the Earth Sciences: Principles and Applications, Miner Assoc Canada Short Course Series,
1287 Ottawa, Ontario, Canada, 29, 239-243
- 1288 [Vicente, J.-C., Sequeiros, F., Valdivia, M., Zavala, J.](#), 1982. El sobre-escurrimiento de Cincha-
1289 Lluta: elemento del accidente mayor andino al NW de Arequipa. Bol Soc Geol Perú 61: 67-
1290 99
- 1291 [Walker, B.A., Klemetti, E.W., Grunder, A.L., Dilles, J.H., Tepley, F.J., Giles, D.](#), 2013.
1292 Crystal reaming during the assembly, maturation, and waning of an eleven-million-year
1293 crustal magma cycle: thermobarometry of the Aucanquilcha Volcanic Cluster. Contrib
1294 Mineral Petrol 165, 4: 663-682, doi: 10.1007/s00410-012-0829-2
- 1295 [Wegner, W., Ruprecht, P.](#), 2003. Volcanic Geology and Valley History of Rio Chili Canyon,
1296 Arequipa (Southern Peru). Diploma Mapping Thesis, University Göttingen (unpubl.): 83 pp
- 1297 [Wilson, J.J., García, W.](#), 1962. Geología de los cuadrángulos de Pachía y Palca. Com. Carta
1298 Geol. Nac., Boletín, 4, 81 p.
- 1299 [Wilson, M.](#), 1986. Igneous petrogenesis: Unwyn Hyman, London, 456 pp
- 1300 [Wörner, G., Harmon, R.S., Davidson, J.P., Moorbath, S.](#), 1988. The Nevados de Payachata
1301 volcanic region 18°S/69°W, N. Chile). I. Geological, geochemical, and isotopic observations.
1302 Bull Volcanol 30: 287-303
- 1303 [Wörner, G., Mamani, M., Blum-Oeste, M.](#), 2018. Magmatism in the Central Andes. Elements
1304 14: 237-244. Doi: 10.2138/gselements.14.4.237

1305

1306 **Tables captions**

1307 **Table 1.** Characteristics of large volcanic clusters (LVCs) and comparison with compound
1308 volcanoes and individual composite stratocones in the Andean CVZ and elsewhere.

1309 **Table 2.** $^{40}\text{Ar}/^{39}\text{Ar}$ and U/Pb ages of the large Chachani volcano cluster C-LVC and the
1310 neighbouring Yura tuffs.

1311 **Table 3.** Summary of growth stages, eruptive rates, mineral assemblages, and SiO₂, K₂O
1312 content in lavas from the C-LVC.

1313 **Table 4.** Results of calculation using morphometric parameters for the C-LVC and each of its
1314 edifices.

1315 **Table 5.** Petrographic characteristics of lavas from the twelve C-LVC edifices, and of Pre-
1316 Chachani and Chachani base lavas. Pl: plagioclase, opx: orthopyroxene, cpx: clinopyroxene,
1317 amph: amphibole, bi: biotite, mgt: magnetite. % values in parentheses represents the
1318 percentage of crystal content as phenocrysts (>500 μm) and micro-phenocrysts (100-500 μm)
1319 and microlites (<100 μm) in the groundmass.

1320

1321 **Figures captions**

1322 **Figure 1.** A) SiO_2 composition versus duration, and B) Volume versus magma eruptive rates
1323 plotted for the Chachani Volcano Cluster and other clusters, compared to compound volcanoes
1324 (massifs) and individual composite volcanoes in CVZ, and other volcanic clusters worldwide.
1325 CVZ individual composite cones and compound volcanoes (red triangles) include: San Pedro
1326 (O'Callaghan and Francis, 1986), Ollagüe (Feeley et al., 1993; Feeley and Davidson, 1994),
1327 Lascar (Mathews et al., 1994), Llullaillaco (Richards and Villeneuve, 2011), El Misti (Thouret
1328 et al., 2001), Ubinas (Thouret et al., 2005), Tancitaro (Ownby et al., 2007), Parinacota (Hora et
1329 al., 2007), Auncanquilcha (Klemetti and Grunder, 2007), Uturuncu (Sparks et al., 2008; Muir
1330 et al., 2015) and Ampato-Sabancaya (Samaniego et al., 2016). Large volcano clusters, fields or
1331 complexes (blue triangles) encompass: Pichincha massif (Robin et al., 2010; Samaniego et al.,
1332 2010), Unzen (Hoshizumi et al., 1999), Taápaca (Clavero et al., 2004), and Coropuna cluster
1333 (Mariño et al., 2020). And for the purpose of comparison although the crust thickness is thinner
1334 than CVZ crust: Mt. Baker field (Hildreth et al., 2003), Mt. Adams field (Hildreth and
1335 Lanphere, 1994), and Mt. Mazama field (Bacon and Lanphere, 2006). Average eruptive rate
1336 has been calculated using bulk volume of erupted material for each of the volcanic systems.
1337 Two black dots with associated error range indicate the C-LVC maximum and minimum
1338 volume estimates.

1339 **Figure 2.** Topographic map illustrating the location of the Chachani volcano complex and the
1340 regional geodynamic setting. AOH: Andagua-Orcopampa-Huambo monogenetic field; CLF:
1341 Chivay Lava Field. Subduction zone and convergence rate between Nazca and South American
1342 plates are indicated. Continuous and dashed lines delineate the extent of the Pleistocene-
1343 Holocene Frontal arc and the Early Quaternary volcano range, respectively. The map also

1344 shows the monogenetic field of Andahua-Orcopampa-Huambo, and the principal rivers and
1345 cities or towns. Relief of image taken from Arc Map World Imagery Service. Topography and
1346 bathymetry data are from the SRTM15_PLUS version 1.0 data set.

1347 **Figure 3.** Geological and structural map of the C-LVC in the Arequipa area. **A.** The
1348 morphotectonic scheme indicates two domains defined by [Carlotto et al. \(2009\)](#), combined with
1349 volcano-structural features (after [Aguilar, 2015](#)). Lithological data was taken from
1350 GEOCATMIN, INGEMMET (2014). **B.** Copernicus Sentinel-2 satellite image showing
1351 volcanic edifices composing the C-LVC. **C.** Sketch diagram showing how we interpret the
1352 transpressional tectonic setting in which the C-LVC has grown. Intersections (displayed in
1353 grey) of normal faults N80° that offset the strike-slip N130° faults together with Riedel N10°
1354 and 40° may act as preferential paths for C-LVC magmas. Graphic scale indicates that the
1355 diagram has been depicted at the scale of the map 3B.

1356 **Figure 4.** Generalized map on DEM showing two, Old- and Young Edifice groups totaling
1357 twelve edifices forming the C-LVC and Pre-Chachani rocks. Red spots indicate the location of
1358 samples used for chemical analysis. Black dots indicate location of samples with $^{40}\text{Ar}/^{39}\text{Ar}$
1359 (black text with white frame) and U/Pb (white text with black frame) ages expressed in ka. The
1360 initiation and end of both geological cross sections NNE-SSW and NNW-SSE ([Fig. 5](#)) are
1361 shown. Generalized stratigraphic section of the C-LVC (right-hand side).

1362 **Figure 5.** Schematic geological sections showing the postulated structures and bedrock surface
1363 underneath the C-LVC. **A.** Cross section from the old Nocarane volcano (NNW) to the Cabreria
1364 dome (SSE) through the youngest Nevado Chachani cone. **B.** Cross section from Nocarane
1365 (NNE) to the Airport-Potrero dome cluster through the La Horqueta cumulo-dome. These two
1366 profiles are located with white dots on figure 6.

1367 **Figure 6.** 3-D diagrams showing how we reconstructed the ‘pre-Chachani’ palaeo-topography
1368 based on DEM and interpolation of coordinates and elevation dataset from the geological map
1369 using Surfer software ([Fig. 4](#)). White, dashed lines indicate both cross sections shown in [Figure](#)
1370 [5](#). The interval between the contours lines is 200 meters.

1371 **Figure 7.** Observed textures in thin sections of the C-LVC lavas. Photomicrographs in plane-
1372 polarized light suggest features attributed to magma mixing processes in lavas, as seen in: **(A)**
1373 Light and brown colored groundmass in Volcancillo; **(B)** Microlithic and glassy groundmass in
1374 Estribo stratovolcano. Back Scattered Electron images (BSE) showing the typical textures
1375 observed in the C-LVC samples; **(C)** Spongy cellular texture “sieve” in plagioclase; **(D)**

1376 Pervasive resorption in amphibole; **(E)** Breakdown texture in biotite with orthopyroxene
1377 recrystallization; **(F)** resorption and recrystallization in olivine.

1378 **Figure 8.** Compositional diversity of magmas of C-LVC lavas in the diagram SiO₂ versus K₂O
1379 (data from this work and Mamani et al., 2010), after [Peccerillo and Taylor \(1976\)](#), compared
1380 with available datasets of Pleistocene-Holocene lavas and lava-domes of the Andean CVZ
1381 ([Wörner et al., 2018](#); [Mamani et al., 2010](#); grey dots).

1382 **Figure 9.** Variations in magma compositions as a function of time for all edifices of the C-
1383 LVC. The vertical position of samples illustrates their relative stratigraphic positions based on
1384 ⁴⁰Ar/³⁹Ar ages. * Age of Yura Tuffs emplaced between Pre-Chachani and C-LVC edifices.

1385 **Figure 10.** Multi-element diagrams normalized to primitive mantle ([Sun and McDonough,](#)
1386 [1989](#)) showing trace element patterns of the C-LVC lava samples. **A.** Old Edifice group, **B.**
1387 Young Edifice group. The grey backgrounds show the available datasets of Pleistocene-
1388 Holocene lavas and lava-domes of the Andean CVZ ([Wörner et al., 2018](#); [Mamani et al., 2010](#)).

1389 **Figure 11.** Plots of major and trace element ratios for the C-LVC, and the La Joya Ignimbrite
1390 (LJI, *c.* 4.9 Ma) and Arequipa Airport Ignimbrite (AAI, *c.* 1.62-1.66 Ma) for the purpose of
1391 comparison with post-caldera C-LVC magmas. Major elements for C-LVC, LJI and AAI show
1392 a similar pattern using silica content. Trace element (Ba, Th and Dy/Yb ratios) allow us to
1393 correlate AAI and C-LVC magmas and distinguish those from the LJI magma.

1394 **Figure 12.** Variations in trace element signatures versus silica content observed in the C-LVC
1395 lavas compared to Pleistocene-Holocene lavas and lava domes in the Central Andes. **(A)** Ba/Sr
1396 plotted with respect to wt.% SiO₂. **(B)** Sr/Y plotted with respect to wt.% SiO₂. **(C)** Dy/Yb
1397 plotted with respect to wt.% SiO₂. **(D)** Sm/Yb plotted with respect to wt.% SiO₂. Arrows
1398 indicate compositional variations caused by the distinct preference for certain trace elements in
1399 the different residual mineral phases during fractional crystallization and/or crustal melting and
1400 assimilation. Abbreviations are as follows: cpx= clinopyroxene; plag= plagioclase feldspar.
1401 Grey dots represent the available dataset for the frontal arc of CVZ ([Wörner et al., 2018](#);
1402 [Mamani et al., 2010](#)).

1403 **Figure 13.** Plots of Ni versus Rb for lavas from C-LVC. The plots show a scattered negative
1404 correlation of compatible elements (Ni) with incompatible element (Rb) suggest an important
1405 role of magma mixing in the C-LVC evolution.

1406 **Figure 14.** **A)** Diagram FeO (wt. %) vs An (anorthite), displaying variations of plagioclase and
1407 their trend suggesting the influence of magma mixing/mingling. The plots show small variation
1408 of FeO and anorthite for phenocrysts. On the other hand, microlites and crystal rims show
1409 considerable variations indicating hotter, less dense recharge in the magma chamber and/or
1410 heating event prior to the eruptive event. **B)** Mg# versus ^{IV}Al and **C)** ^{IV}Al versus total
1411 displaying variation of amphibole composition.

1412 **Figure 15.** Trace element signatures in the C-LVC lavas for the purpose of comparison with
1413 available datasets of the Andean CVZ magmas ([Wörner et al., 2018](#); [Mamani et al., 2010](#); grey
1414 dots and grey background). **(A)** Sr/Y ratios plotted with respect to wt.% SiO₂. **(B)** Ratios of
1415 Dy/Yb plotted with respect to wt.% SiO₂. **(C)** Dy/Yb ratios plotted with respect to Sm/Yb. **(D)**
1416 Ratio of Sm/Yb plotted with respect to stratigraphic position; the gray box represents the range
1417 of Sm/Yb ratio of Quaternary lavas in the Central Andes. Overall, C-LVC lavas fall into
1418 intermediate values compared to the analyzed Andean CVZ magmas of Quaternary age.

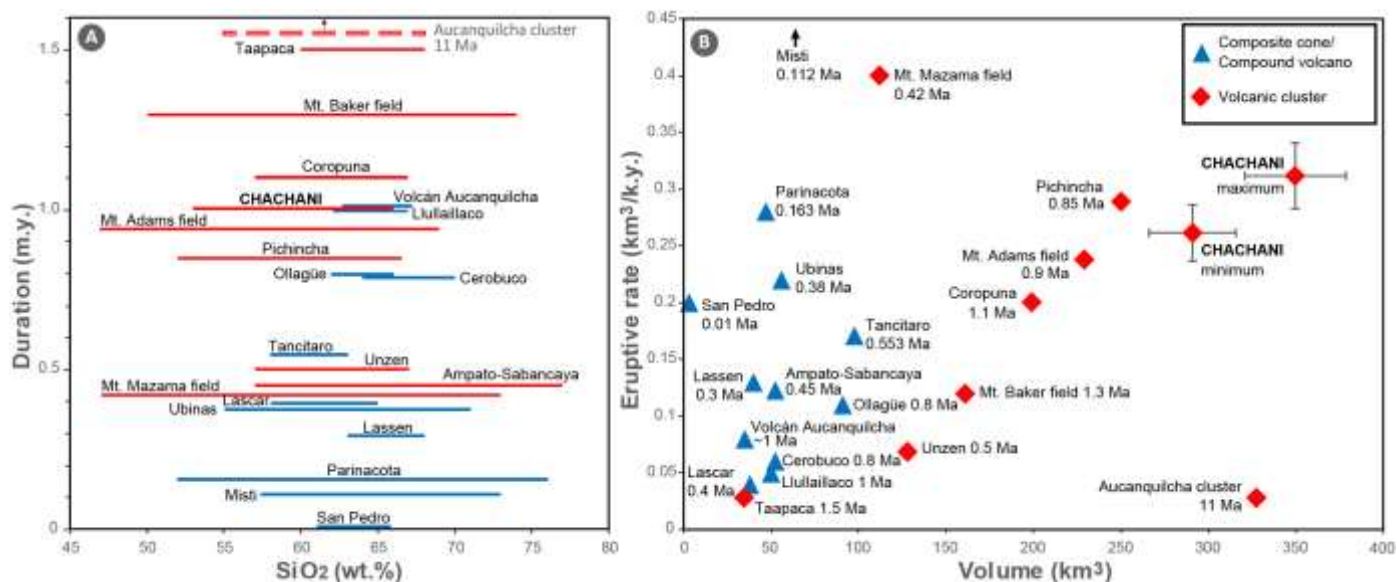


Figure 1. A) SiO₂ composition versus duration, and B) Volume versus magma eruptive rates plotted for the Chachani Volcano Cluster and other clusters, compared to compound volcanoes (massifs) and individual composite volcanoes in CVZ, and other volcanic clusters worldwide. CVZ individual composite cones and compound volcanoes (red triangles) include: San Pedro (O’Callaghan and Francis, 1986), Ollagüe (Feeley et al., 1993; Feeley and Davidson, 1994), Lascar (Matthews et al., 1994), Llullaillaco (Richards and Villeneuve, 2011), El Misti (Thouret et al., 2001), Ubinas (Thouret et al., 2005), Tancitaro (Ownby et al., 2007), Parinacota (Hora et al., 2007), Aucanquilcha (Klemetti and Grunder, 2007), Uturunco (Sparks et al., 2008; Muir et al., 2015) and Ampato-Sabancaya (Samaniego et al., 2016). Large volcano clusters, fields or complexes (blue triangles) encompass: Pichincha massif (Robin et al., 2007; Samaniego et al., 2010), Unzen (Hoshizumi et al., 1999), Taápaca (Clavero et al., 2004), and Coropuna cluster (Mariño et al., 2020). And for the purpose of comparison although the crust thickness is thinner than CVZ crust: Mt. Baker field (Hildreth et al., 2003), Mt. Adams field (Hildreth and Lanphere, 1994), and Mt. Mazama field (Bacon and Lanphere, 2006). Average eruptive rate has been calculated using bulk volume of erupted material for each of the volcanic systems. Two black dots with associated error range indicate the C-LVC maximum and minimum volume estimates.

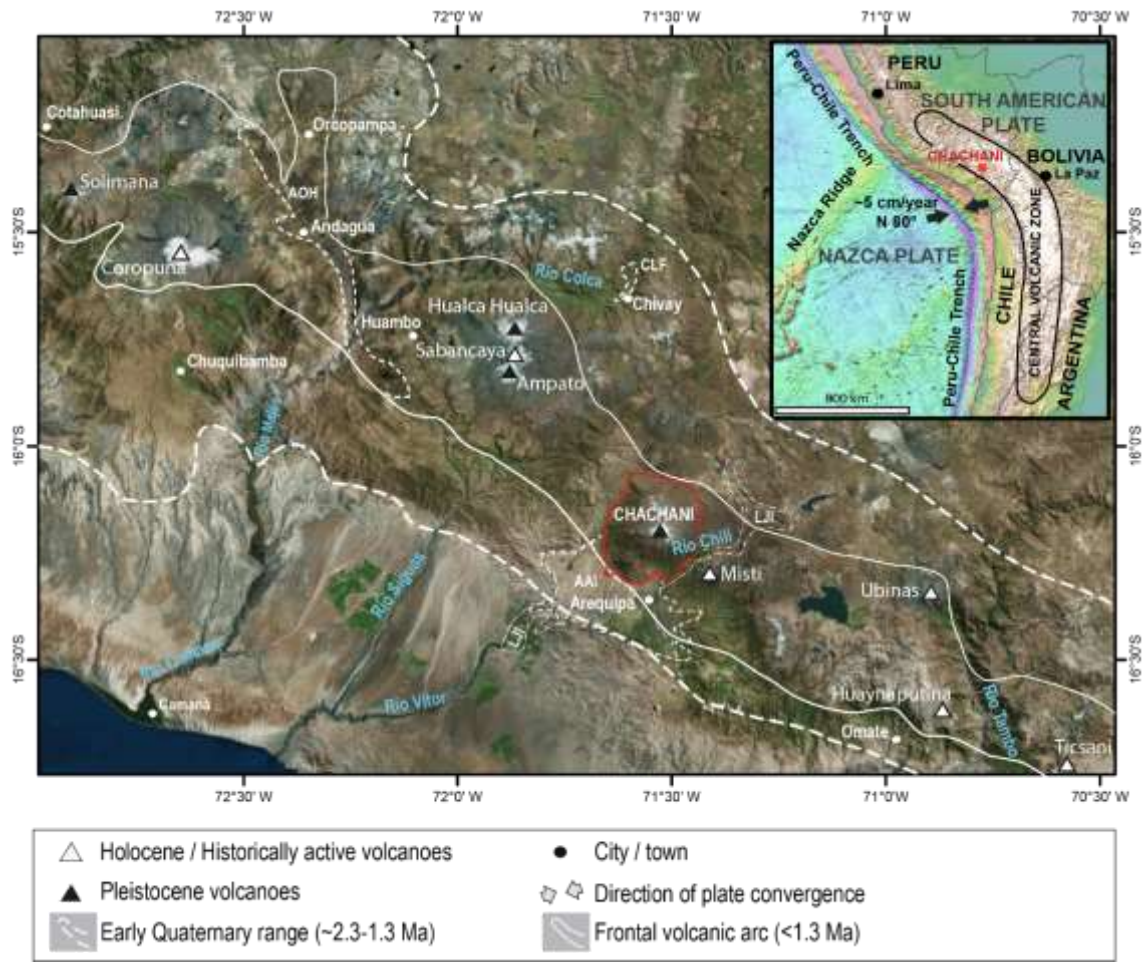


Figure 2. Topographic map illustrating the location of the Chachani volcano complex and the regional geodynamic setting. AOH: Andagua-Orcopampa-Huambo monogenetic field; CLF: Chivay Lava Field. Subduction zone and convergence rate between Nazca and South American plates are indicated. Continuous and dashed lines delineate the extent of the Pleistocene-Holocene Frontal arc and the Early Quaternary volcano range, respectively. The map also shows the monogenetic field of Andahua-Orcopampa-Huambo, and the principal rivers and cities or towns. Relief of image taken from Arc Map World Imagery Service. Topography and bathymetry data are from the SRTM15_PLUS version 1.0 data set.

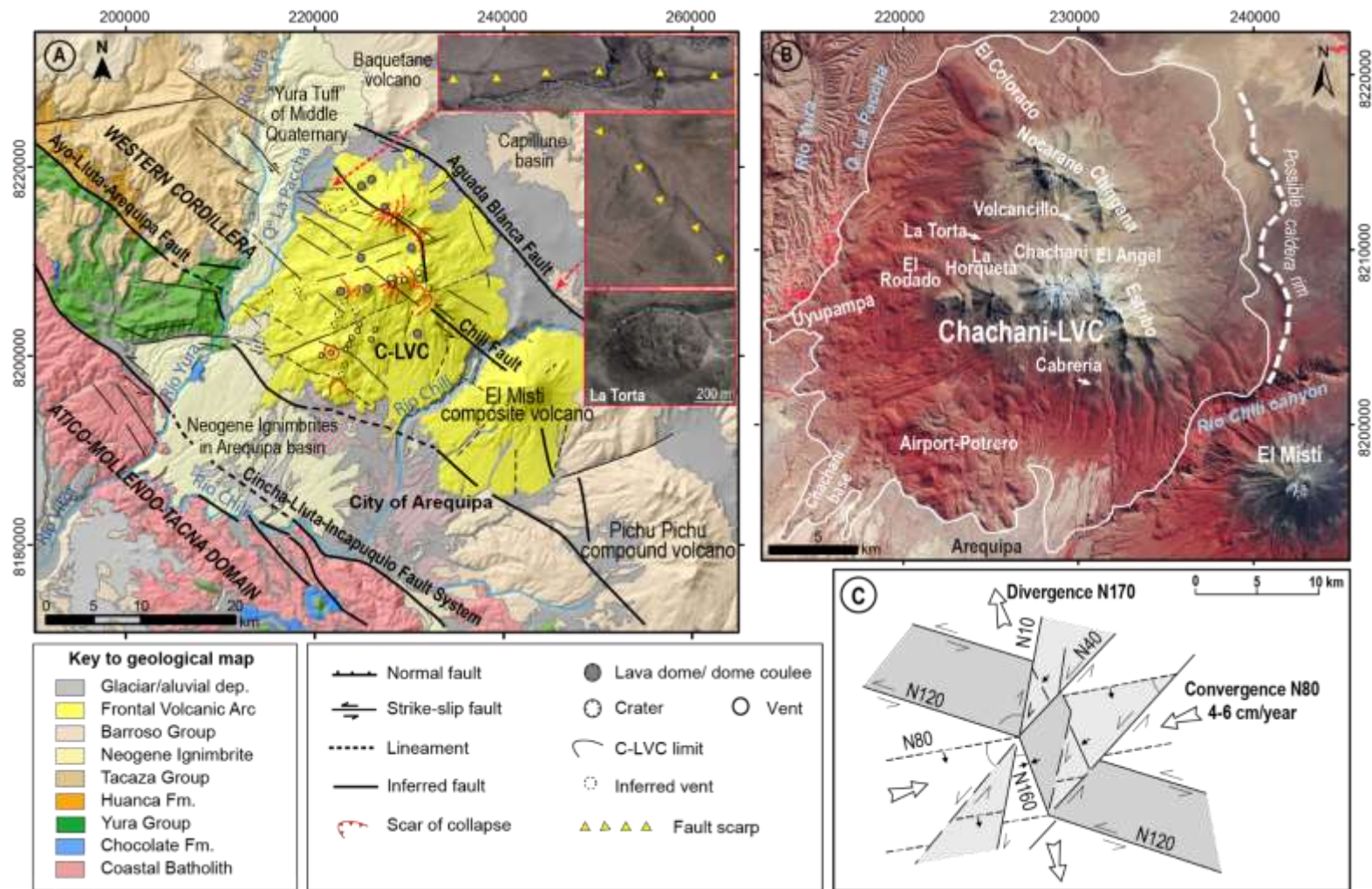


Figure 3. Geological and structural map of the C-LVC in the Arequipa area. **A.** The morphotectonic scheme indicates two domains defined by [Carlotto et al. \(2009\)](#), combined with volcano-structural features (after [Aguilar, 2015](#)). Lithological data was taken from GEOCATMIN, INGEMMET (2014). **B.** Satellite image showing volcanic edifices composing the C-LVC. **C.** Sketch diagram showing how we interpret the transpressional tectonic setting in which the C-LVC has grown. Intersections (displayed in grey) of normal faults N80° that offset the strike-slip N130° faults together with Riedel N10° and 40° may act as preferential paths for C-LVC magmas. Graphic scale indicates that the diagram has been depicted at the scale of the map 3B.

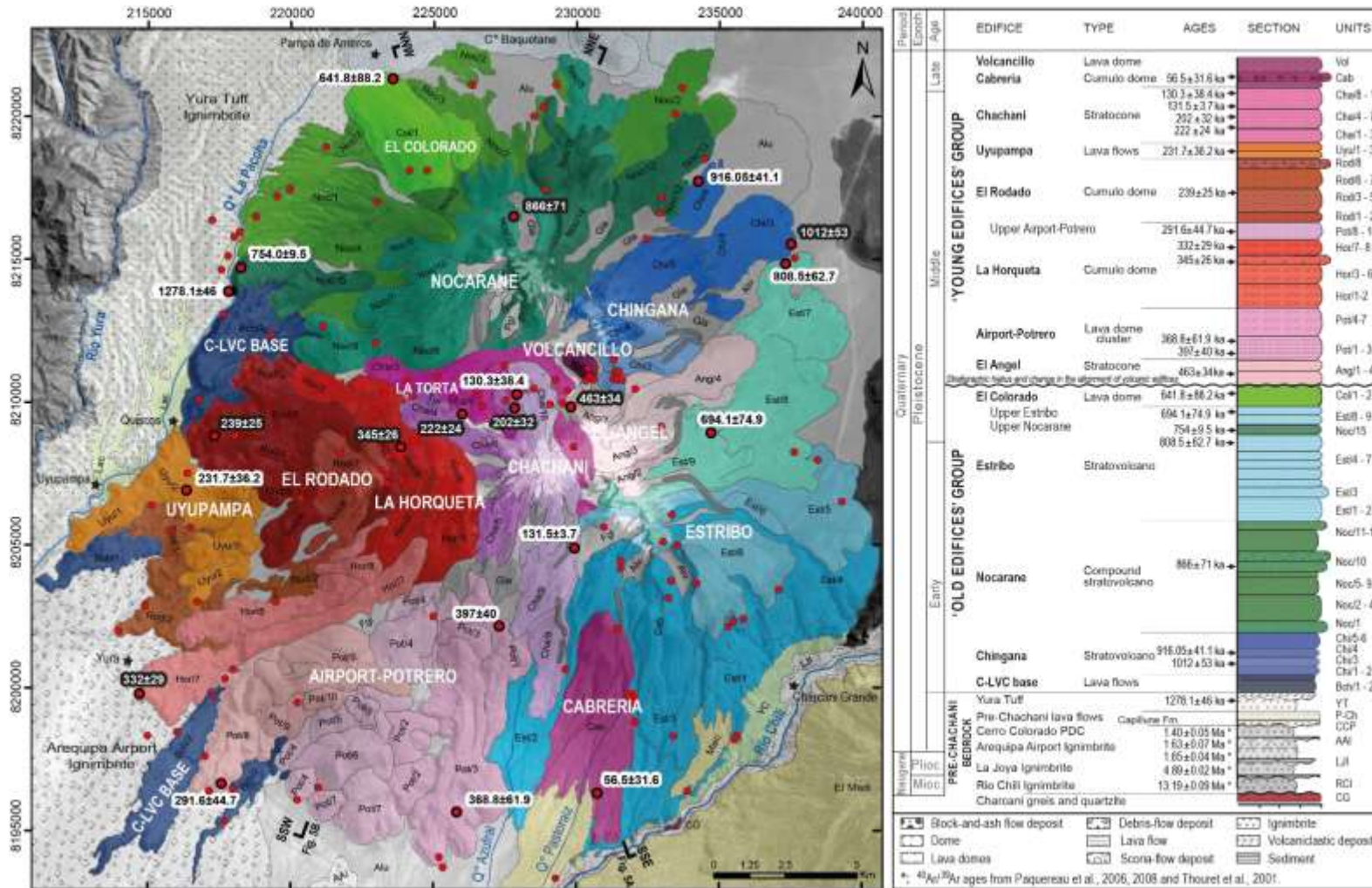


Figure 4. Generalized map on DEM showing two, ‘Old-’ and ‘Young edifices’ groups totaling twelve edifices forming the C-LVC and Pre-Chachani rocks. Red spots indicate the location of samples used for chemical analysis. Black dots indicate location of samples with ⁴⁰Ar/³⁹Ar (black text with white frame) and U/Pb (white text with black frame) ages expressed in ka. The initiation and end of both geological cross sections NNE-SSW and NNW-SSE (Fig. 5) are shown. Generalized stratigraphic section of the C-LVC (right).

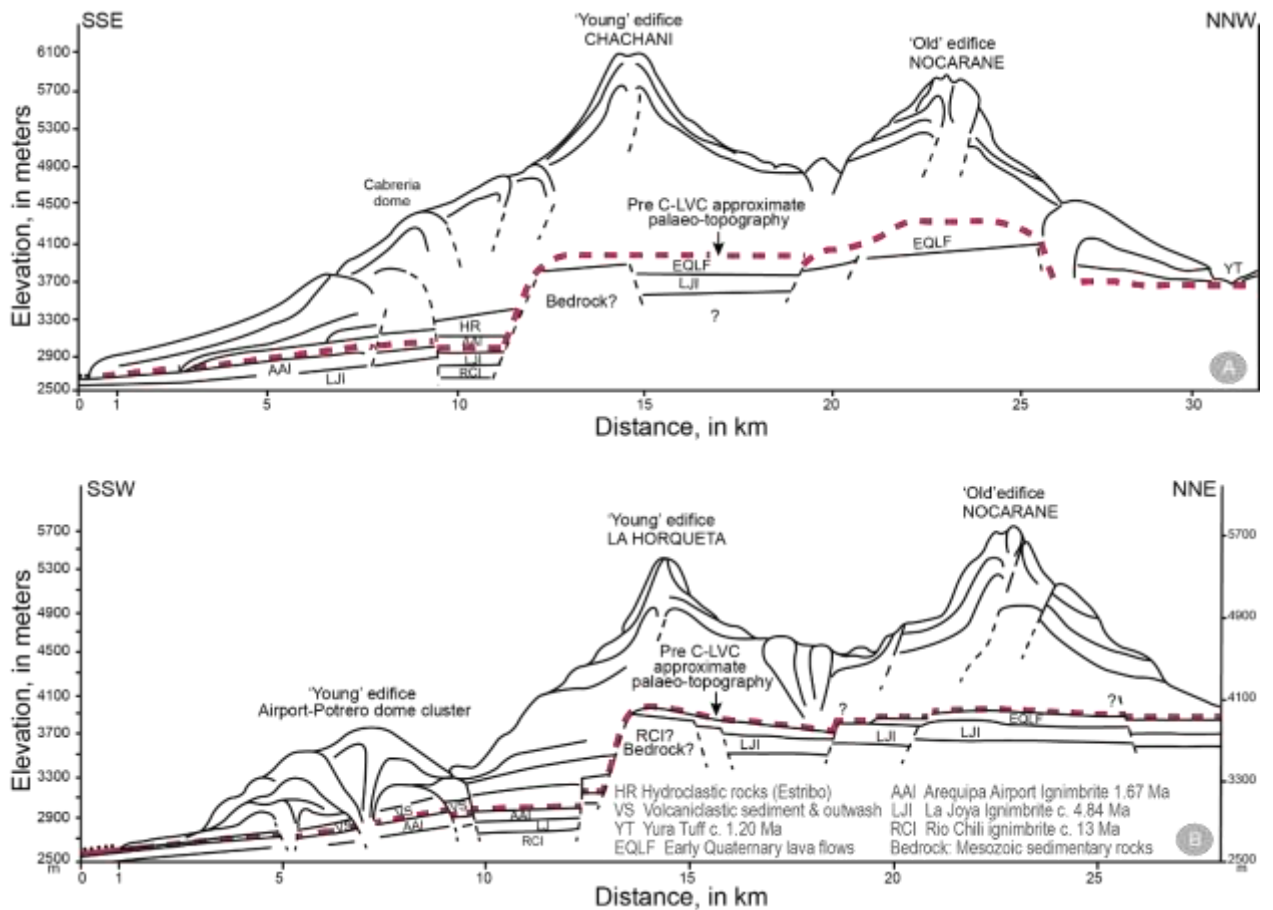


Figure 5. Schematic geological sections showing the postulated structures and bedrock surface underneath the C-LVC. **A.** Cross section from the old Nocarane volcano (NNW) to the 'young' Cabreria dome (SSE) through the youngest Nevado Chachani cone. **B.** Cross section from Nocarane (NNE) to the 'young' Airport dome cluster through the 'young' La Horqueta cumulo-dome. These two profiles are located with white dots on figure 6.

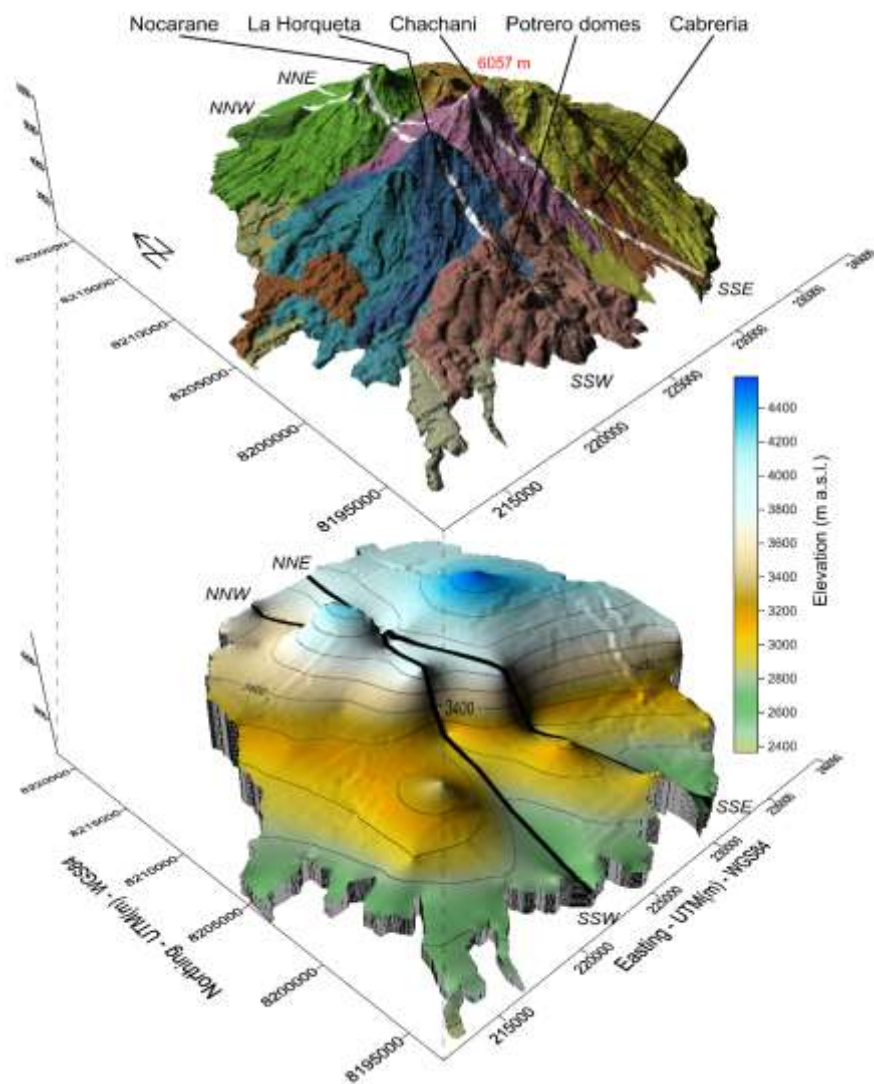


Figure 6. 3-D diagrams showing how we reconstructed the pre-Chachani palaeo-topography based on DEM and interpolation of coordinates and elevation dataset from the geological map using Surfer software (Fig. 4). White or black bold lines indicate both cross sections shown in Figure 5. The interval between the contours lines is 200 meters. Colors code on the geological map: same as figure 4.

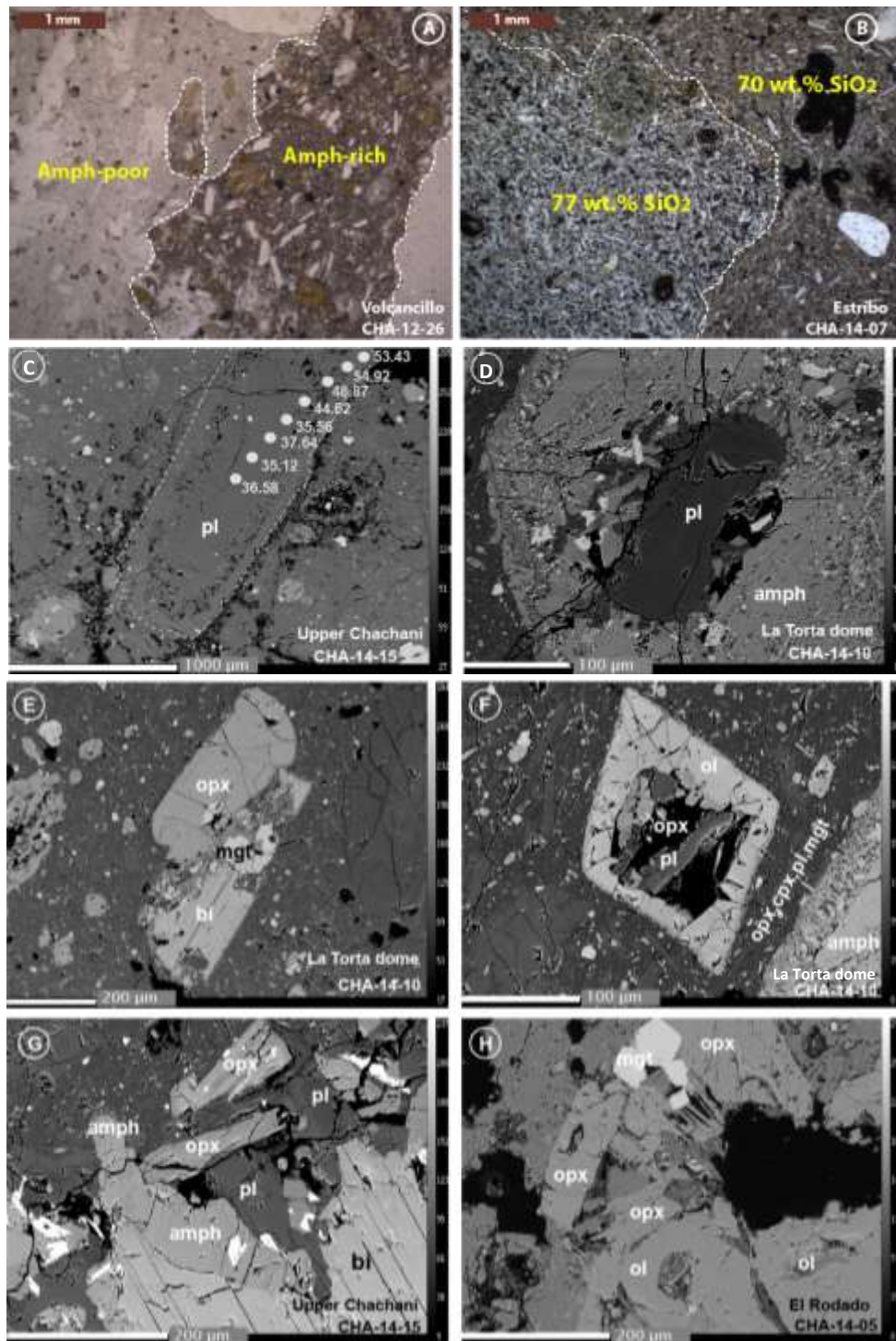


Figure 7. Observed textures in thin sections of the C-LVC lavas. Photomicrographs in plane-polarized light suggest features attributed to magma mixing processes in lavas, as seen in: (A) Light and brown colored groundmass in Volcancillo; (B) Microlithic and glassy groundmass in Estribo stratovolcano. Back Scattered Electron images (BSE) showing the typical textures observed in the C-LVC samples; (C) Spongy cellular texture “sieve” in plagioclase; (D) Pervasive resorption in amphibole; (E) Breakdown texture in biotite with orthopyroxene recrystallization; (F) resorption and recrystallization in olivine

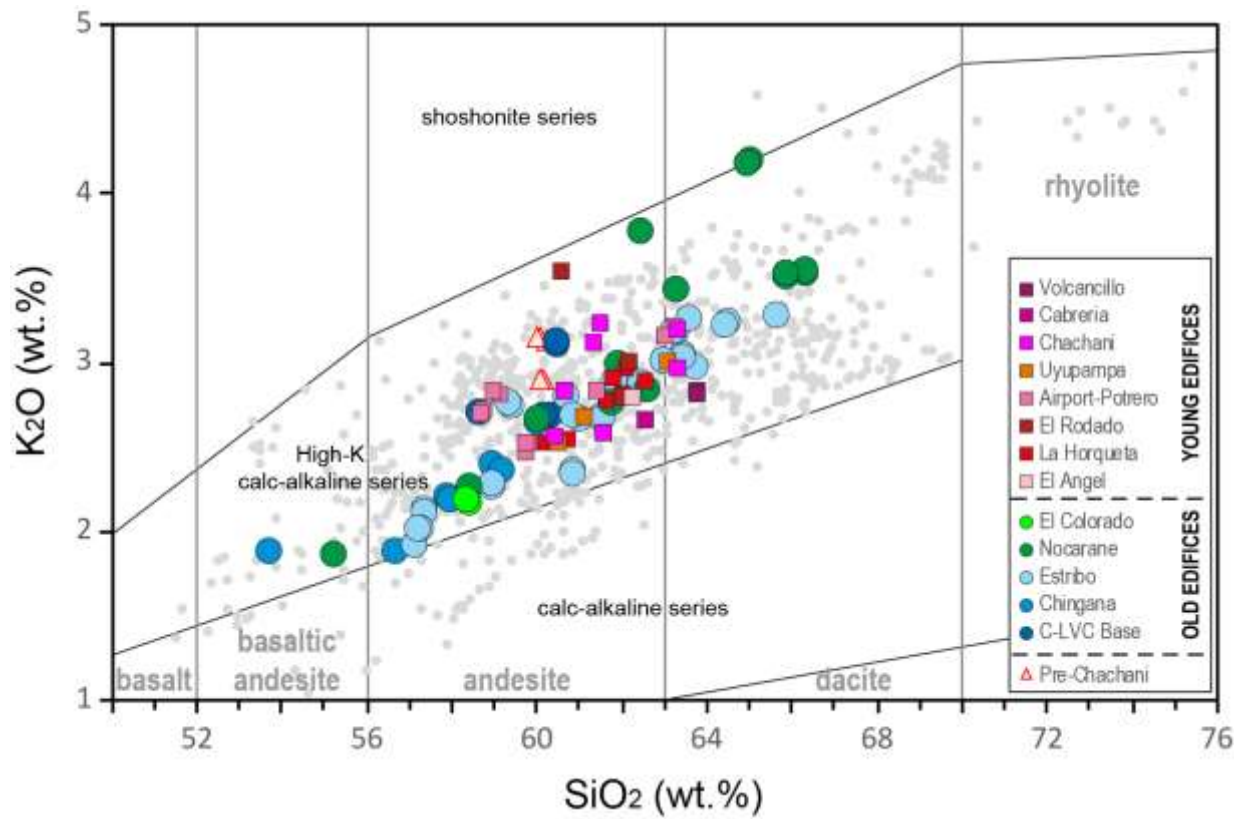


Figure 8. Compositional diversity of magmas of C-LVC lavas in the diagram SiO₂ versus K₂O (data from this work and Mamani et al., 2010), after Peccerillo and Taylor (1976), compared with available datasets of Pleistocene-Holocene lavas and lava-domes of the Andean CVZ (Wörner et al., 2018; Mamani et al., 2010; grey dots).

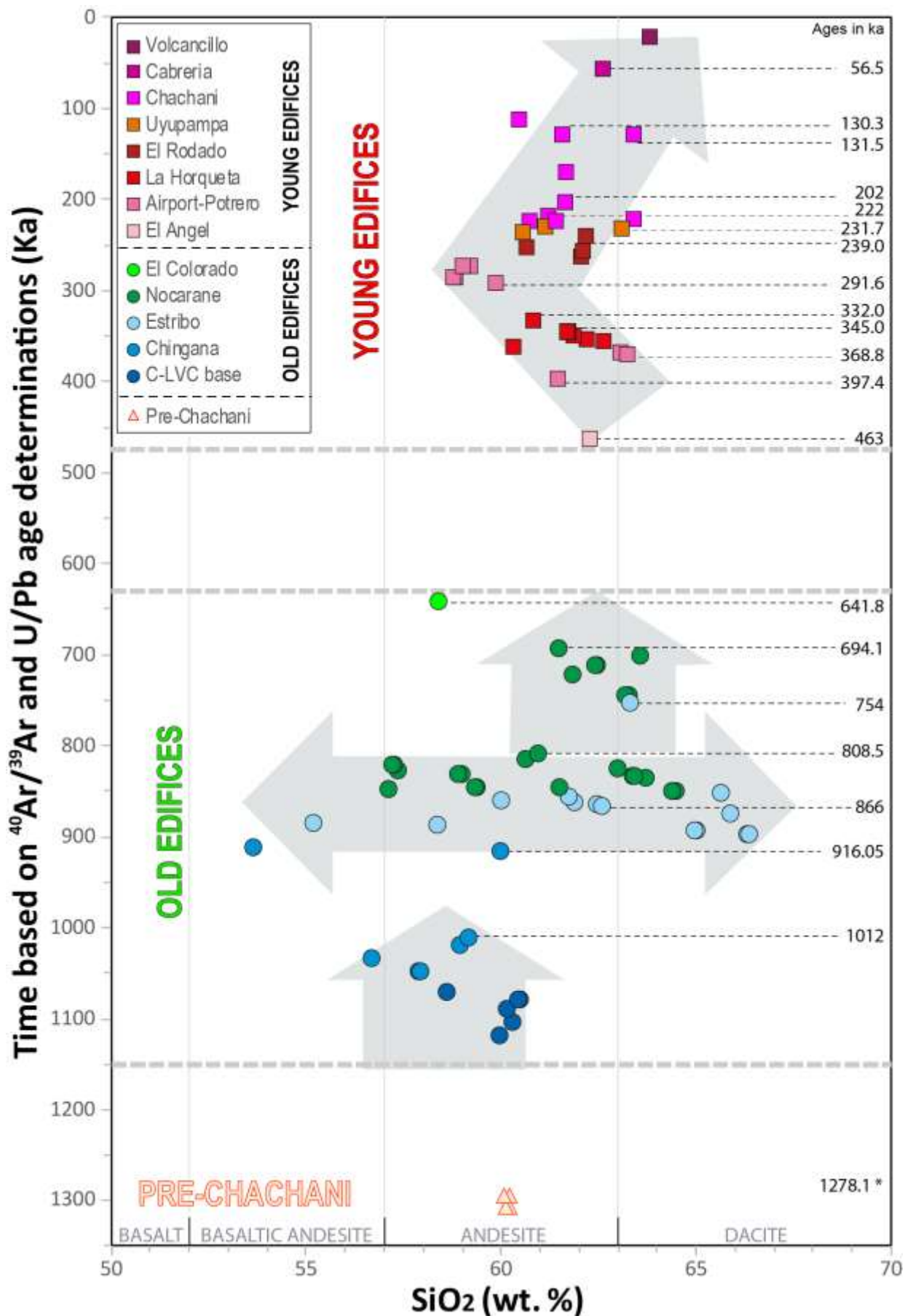


Figure 9. Variations in magma compositions as a function of time for all edifices of the C-LVC. The vertical position of samples illustrates their relative stratigraphic positions based on $^{40}\text{Ar}/^{39}\text{Ar}$ ages. * Age of Yura Tuffs emplaced between Pre-Chachani and C-LVC edifices.

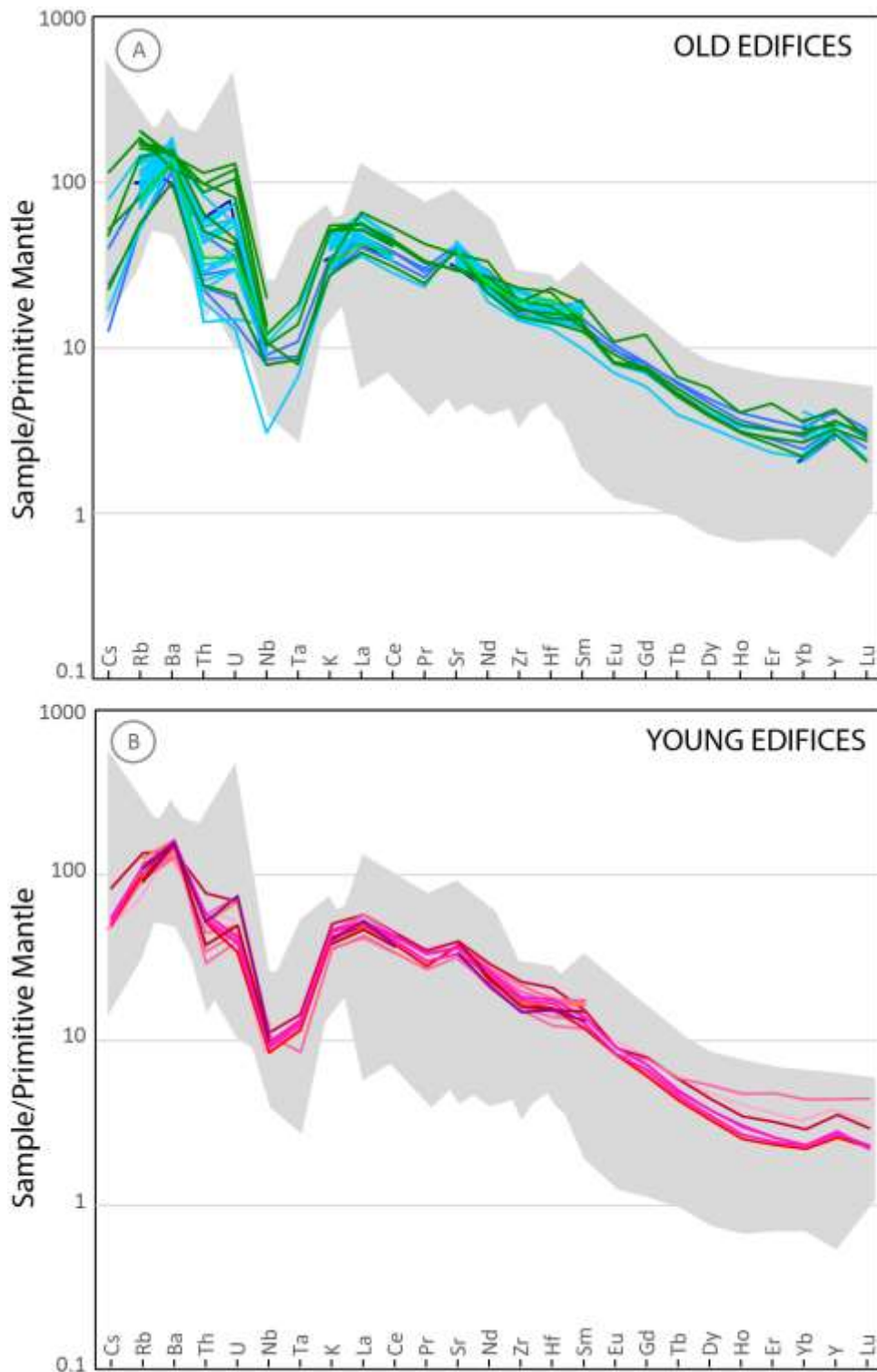


Figure 10. Multi-element diagrams normalized to primitive mantle (Sun and McDonough, 1989) showing trace element patterns of the C-LVC lava samples. **A.** ‘Old’ edifices, **B.** ‘Young’ edifices. The grey backgrounds show the available datasets of Pleistocene-Holocene lavas and lava domes of the Andean CVZ (Wörner et al., 2018; Mamani et al., 2010).

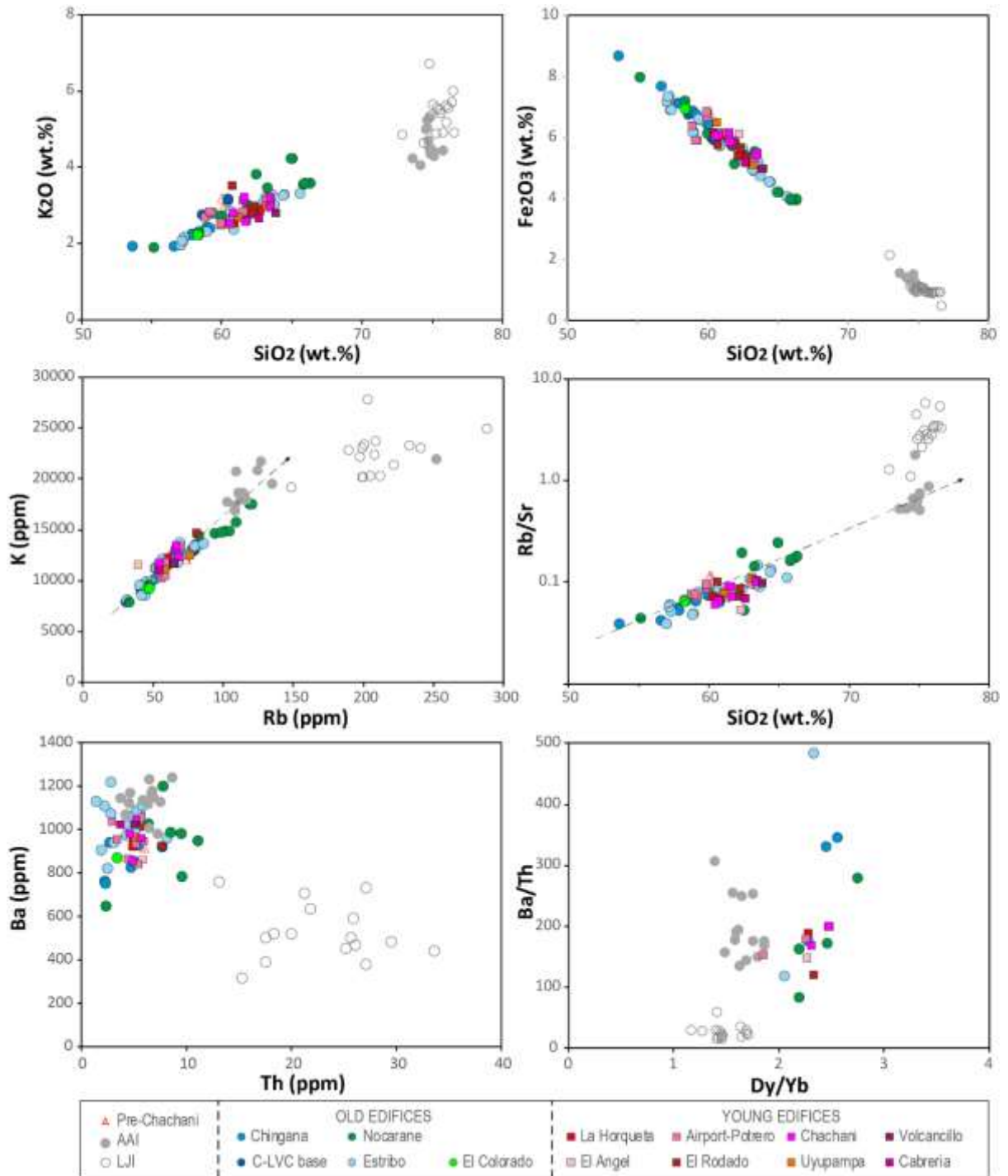


Figure 11. Plots of major and trace element ratios for the C-LVC, and the La Joya Ignimbrite (LJI, c.4.9 Ma) and Arequipa Airport Ignimbrite (AAI, c.1.62-1.66 Ma) for the purpose of comparison with post-caldera C-LVC magmas. Major elements for C-LVC, LJI and AAI show a similar pattern using silica content. Trace element (Ba, Th and Dy/Yb ratios) allow us to correlate AAI and C-LVC magmas and distinguish those from the LJI magma.

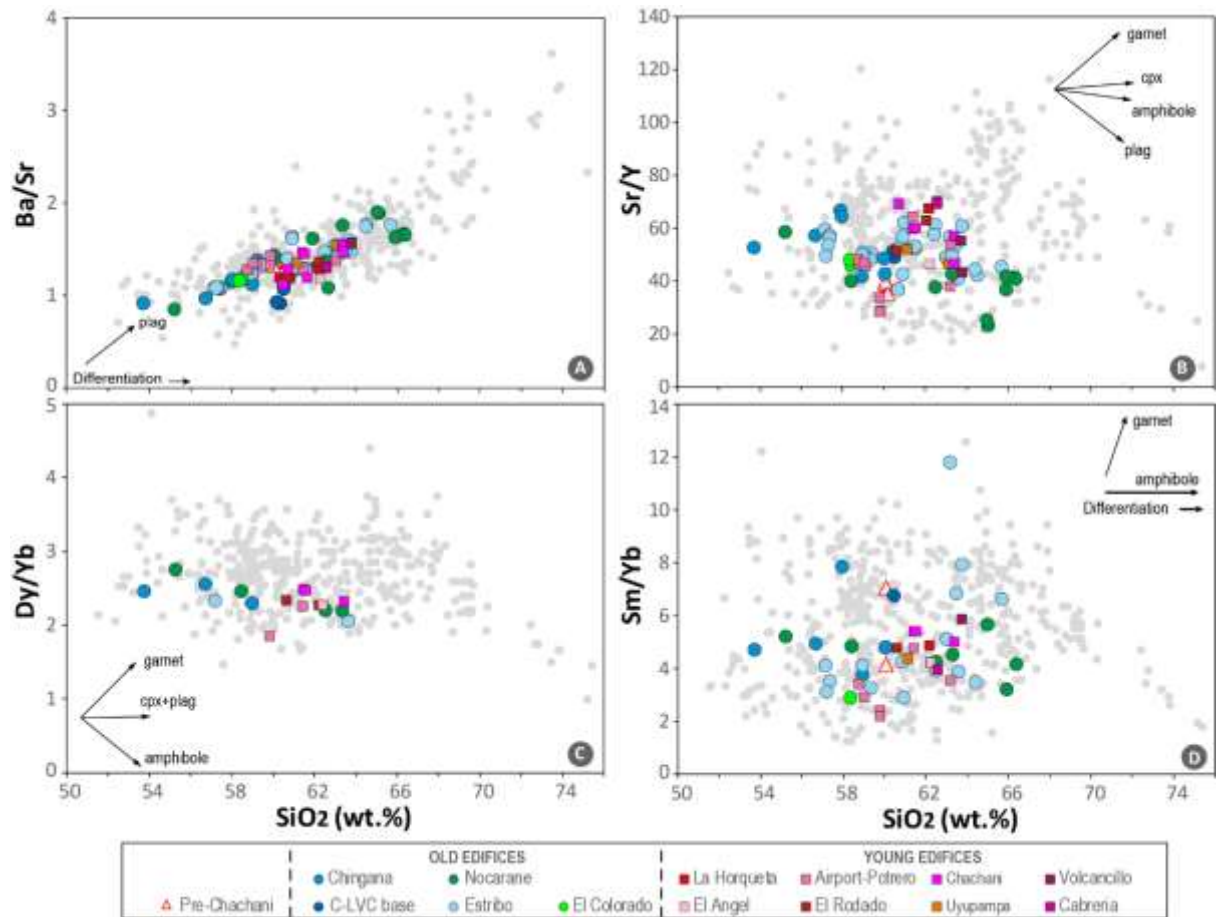


Figure 12. Variations in trace element signatures versus silica content observed in the C-LVC lavas compared to Pleistocene-Holocene lavas and lava domes in the Central Andes. **(A)** Ba/Sr plotted with respect to wt% SiO₂. **(B)** Sr/Y plotted with respect to wt% SiO₂. **(C)** Dy/Yb plotted with respect to wt% SiO₂. **(D)** Sm/Yb plotted with respect to wt% SiO₂. Arrows indicate compositional variations caused by the distinct preference for certain trace elements in the different residual mineral phases during fractional crystallization and/or crustal melting and assimilation. Abbreviations are as follows: cpx= clinopyroxene; plag= plagioclase feldspar. Grey dots represent the available dataset for the frontal arc of CVZ (Wörner et al., 2018; Mamani et al., 2010).

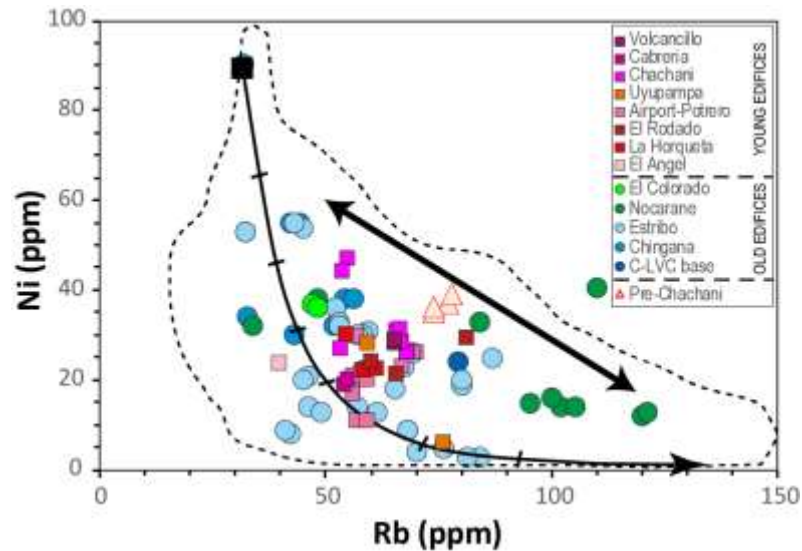


Figure 13. Plots of Ni versus Rb for lavas from C-LVC. The plots show a scattered negative correlation of compatible elements (Ni) with incompatible element (Rb) suggest an important role of magma mixing in the C-LVC evolution.

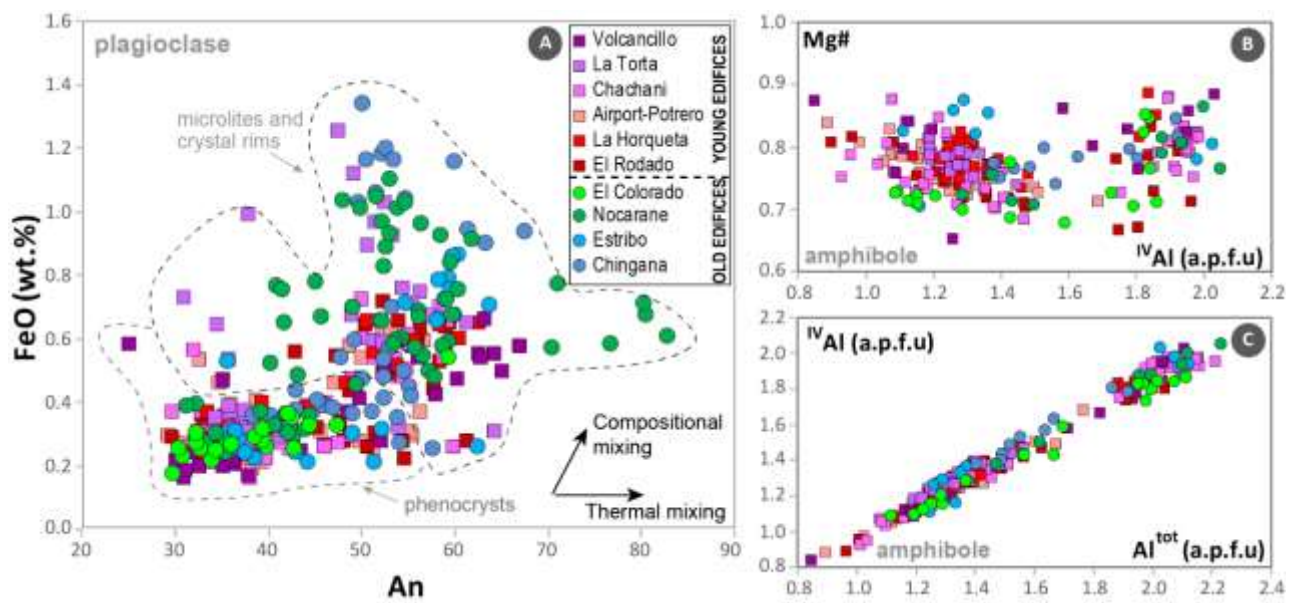


Figure 14. A) Diagram FeO (wt. %) vs An (anorthite), displaying variations of plagioclase and their trend suggesting the influence of magma mixing/mingling. The plots show small variation of FeO and anorthite for phenocrysts. On the other hand, microlites and crystal rims show considerable variations indicating hotter, less dense recharge in the magma chamber and/or heating event prior to the eruptive event. B) Mg# versus $IVAl$ and C) $IVAl$ versus total displaying variation of amphibole composition.

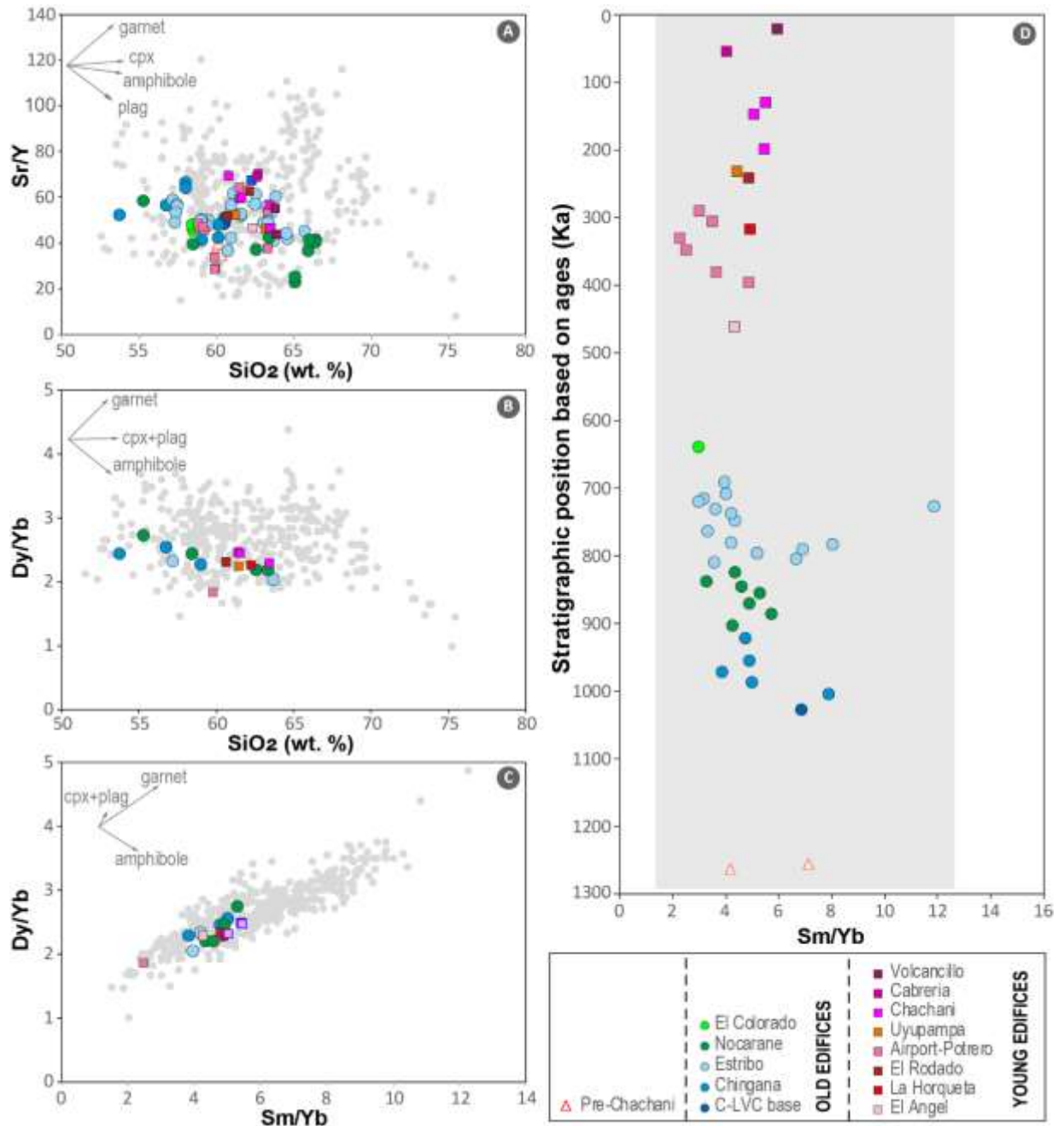


Figure 15. Trace element signatures in the C-LVC lavas for the purpose of comparison with available datasets of the Andean CVZ magmas (Wörner et al., 2018; Mamani et al., 2010; grey dots and grey background). (A) Sr/Y ratios plotted with respect to w% SiO₂. (B) Ratios of Dy/Yb plotted with respect to w% SiO₂. (C) Dy/Yb ratios plotted with respect to Sm/Yb. (D) Ratio of Sm/Yb plotted with respect to stratigraphic position; the gray box represents the range of Sm/Yb ratio of Quaternary lavas in the Central Andes. Overall, C-LVC lavas fall into intermediate values compared to the analyzed Andean CVZ magmas of Quaternary age.

Large volcanic cluster, LVC. Compound volcano (massif)	Surface (km²)	Volume (km³) ± 10%	No. of eruptive centres	Lifetime (Ma)	Eruptive pulses / stages Ma	DRE magma production km³	Bulk magma output rate km³/kyr	Compositional range	Caldera: associated or buried	Reference
Chachani LVC, CVZ, S Peru	580-600	Min c. 290 Max 350 ± 29/35	12	1.27	2: 'old' 1.1-0.6, 'young' 0.4-0.05	198-231 (80% lava flows)	Aver. 0.14-0.22 Peak 0.28-0.3 'Old' group: 'Young' group:	Mafic andesite to dacite	Probably buried	This study: geologic map & DEM Figs. 4, 6: Cross sections Fig. 5
Coropuna LVC, CVZ, S Peru	400-450	135-200	5	1.1	4: 'old' 1.1-0.4, 'young' 0.2-0.0014	130-180 (90% lava flows)	Aver. 0.2 Peak 0.3	Mafic andesite to dacite	Probably buried	Mariño et al., 2020
Ampato (A) – Sabancaya (S) massif, CVZ, S Peru	c. 240-260	A 38-42 S 6-10 Total 44-54	3 1	A 0.4-0.45 S 0.005-0.01	5 Ampato 0.45-0.1 1 Sabancaya 0.01-0.005	40-50	A 0.10-0.12 S 0.6-1.7 (max) Aver. 0.08-0.09	Andesite and dacite	Probably buried?	Samaniego et al., 2016; Thouret et al., 1994; Bromley et al., 2019
Aucanquilcha massif, CVZ, N Chile	c. 80	37	1	1	4	70	Av. 0.04 – 0.10 Peak 0.16	Dacite		Klemetti and Grunder, 2007
Aucanquilcha Cluster, CVZ, N Chile	700	327 ± 20	19	11	3 (1.5 to 3 Myr)	300	Av. 0.03 Peak 0.11-0.22	Mafic andesite to dacite		Grunder et al., 2008; Walker et al, 2013
Lastarria - Cordón del Azufre LVC, CVZ Chile -Argentina	LVC 500 Lastarria 90	45 Lastarria 200 cluster	7	0.6 – <0.3	4 Lastarria 3 Cordón del Azufre	40 180	0.1-0.15 Max 0.33	Andesite and dacite	Yes Current inflation	Naranjo, 1992; Froger et al., 2007
Payachata Parinacota stratovolcanoes, CVZ, N Chile	190 50	Parinacota 46 Pomerape 40	2	0.163	4 Parinacota	40 35	Parinacota 0.25-0.31 (max 0.5-1.2)	Dacite and rhyolite		Wörner et al., 1988; Davidson et al., 1990; Hora et al., 2007
Ollagüe compound volcano, CVZ, N Chile	480	80-90	>7	< 1	4	70-80	Aver. 0.07-0.08	dacite		Feeley & Davidson, 1994
Llullaillaco compound volcano, CVZ, N Chile	150	50-60	4	1.5 – 0.048	2	40-50	Aver. 0.04-0.06	dacite		Richards and Villeneuve, 2001
Taapaca compound volcano, CVZ, N Chile	180-250	35 - 73	4	1.5	4	30-65	0.05 domes; 0.07 comp. volc.	dacite		Clavero et al., 2004
Lascar stratovolcano, CVZ, N Chile	55-185	50-60	3	< 0.43	4	30-40	Aver. 0.02-0.03 Peak 0.14	dacite		Gardeweg et al., 1998 Mathews et al., 1994
For the purpose of comparison										

Mt. Mazama and volcanic field, Cascades, USA	500	58-112	many	0.42	many	100-120	0.42 Peak 0.8 Volc Field 0.07	Mafic andesite to rhyodacite	Crater Lake caldera	Bacon and Lanphere, 2006
Mt. Adams and volcanic field, Cascades, USA	1250	230-400	Many	0.94	many		Aver. 0.24-0.42	Basalt to dacite		Hildreth and Lanphere, 1994
El Misti individual composite cone	105-130	70-83	2	<0.835max <0.112min	4	55-65	Aver. 0.63 Peak 2.1	Andesite to rhyolite	Summit caldera	Thouret et al., 2001 Rivera et al., 2017
Ubinas individual composite cone	65 - 90	55-60	1	0.376 - Present	2	45-55	Aver. 0.17-0.22	Mafic andesite to rhyolite	Summit caldera	Thouret et al., 2005 Rivera et al., 2014
Andean stratocones		69 - 89		< 1 Ma						Karátson et al., 2012

Table 1. Characteristics of large volcanic clusters (LVCs) and comparison with compound volcanoes and individual composite stratocones in the Andean CVZ and elsewhere.

Sample	Edifice	Unit	UTM coordinates		Lithology	Material	Ages, ka $\pm 2\sigma$ ¹ ⁴⁰ Ar/ ³⁹ Ar ² U/Pb
			North	East			
‘Young’ edifice group							
CHA-02-32	Cabrería	Ca-1	8196348	230640	lava	groundmass	56.5 \pm 31.6 ¹
CHA-12-26	Chachani	Cha10	8210279	227958	lava	groundmass	130.3 \pm 38.4 ¹
CHA-08-44	Chachani	Cha8	8204909	230078	lava	groundmass	131.5 \pm 3.7 ¹
CHA-14-15	Chachani	Cha6	8209905	226802	lava	zircon	202 \pm 32 ²
CHA-14-17	Chachani	Cha4	8209523	226089	lava	zircon	222 \pm 24 ²
CHA-02-33	Uyupampa	Uyu-1	8206885	216438	lava	groundmass	231.7 \pm 36.2 ¹
CHA-04-02	Potrero Domes	Dae-8	8196669	217651	lava	plagioclase	291.6 \pm 44.7 ¹
CHA-14-05	El Rodado	Rod5	8208887	217435	lava	zircon	239 \pm 25 ²
CHA-14-02	La Horqueta	Hor7	8199845	214803	lava	zircon	332 \pm 29 ²
CHA-14-19	La Horqueta	Hor5	8208413	223942	lava	zircon	345 \pm 26 ²
CHA-02-04-JC	Potrero domes	Dae3	8195641	225903	lava	groundmass	368.8 \pm 61.9 ¹
CHA-12-05	Potrero Domes	Dae1	8202150	227400	lava	groundmass	397 \pm 40 ¹
CHA-12-24	El Angel	Ang1	8209865	229815	lava	zircon	463 \pm 34 ²
‘Old’ edifice group							
CHA-02-19	El Colorado	Col1	8221403	223762	lava	groundmass	641.8 \pm 88.2 ¹
CHA-02-17	Estribo	Estr10	8208953	234803	lava	groundmass	694.1 \pm 74.9 ¹
CHA-02-06-JC	Nocarane	Noc11	8199784	231938	lava	groundmass	754.0 \pm 9.5 ¹
CHA-02-24	Estribo	Est8	8215060	237388	lava	plagioclase	808.5 \pm 62.7 ¹
CHA-14-12	Nocarane	Noc10	8216424	227893	lava	zircon	866 \pm 71 ²
CHA-02-26	Chingana	Chi4	8217759	234368	lava	groundmass	916.5 \pm 41.1 ¹
CHA-14-06	Chingana	Chi3	8215505	237644	lava	zircon	1012 \pm 53 ²
CHA-08-07*	Yura Tuff		8214022	217998	Pumice	Plagioclase	1278.1 \pm 46 ¹

Table 2. ⁴⁰Ar/³⁹Ar and U/Pb ages of the large Chachani volcano cluster C-LVC and the neighbouring Yura tuffs. Chronology analytical data is presented in ESD Table 3.

Edifice	Age range (ka)	Estimated duration (ka)	Volume (km ³)	Eruptive rate (km ³ /kyr)	Mineral assemblage	SiO ₂ wt% range	K ₂ O (wt%) range
'Young' edifice group							
Volcancillo	? <150?	<50	0.33-0.39	0.006-0.007	Pl ± amp ± bi	63-65	2.5-2.7
Cabrería	56.5 - <130	50?	4.13-4.91	0.082-0.098	Pl ± amp	61-63	2.4-2.6
Chachani	130*-131.5	90-130	30.34-33.20	0.275-0.302	Pl ± opx ± amp ± (biot) Pl ± amp ± px	61-63	2.6-3.3
Uyupampa	231- ?	50-100?	2.36-2.72	0.031-0.036	Pl ± amp ± bi	61-63	2.8-3.0
El Rodado	>400 - <600	200	6.26-9.17	0.031-0.045	Pl ± cpx ± (ol)	60-62	2.5-3.6
La Horqueta	>400 - <600	200	3.24-6.46	0.032-0.064	Pl ± amp ± bi ± (cpx)	60-62	2.5-3.0
Potrero Domes	291 – 396	100	11.22-12.53	0.112-0.125	Pl ± amp ± cpx ± biot	58-63	2.5-3.5
El Angel	640? - 694	60-100	4.86-5.56	0.060-0.069	Pl ± amp ± cpx ± (biot)	61-63	2.7-2.9
'Old' edifice group							
El Colorado	640-642	<50	4.13-6.16	0.082 - 0.123	Pl ± amp ± bi	57-69	2.1-2.3
Estribo	694 - <916	220-250	59.35-63.03	0.252 - 0.268	Pl ± opx ± amp Pl ± opx ± amp ± (biot) Pl ± cpx ± ol	52-66	1.8-3.2
Nocarane	>640 - 808	175-200?	65.53-125.93	0.350 - 0.673	Pl ± amph ± cpx Pl ± amph ± bi Pl ± cpx ± ol	55-66	1.8-4.2
Chingana	916* - 1100?	80-100	32.10-47.40	0.356 - 0.526	Pl ± opx ± cpx ± amph	59-60	1.8-2.8
Chachani base	1100 – 1278	100-200	1.33-3.62	0.009 - 0.024	Pl ± cpx ± (opx)	59-61	2.8-3.2

Table 3. Summary of growth stages, eruptive rates, mineral assemblages, and SiO₂, K₂O content in lavas from the C-LVC.

Name	Min. age (ka)	Max. age (ka)	Observations	Estimated duration (ka)	Min. vol km ³	Max. vol km ³	Eruption rate km ³ /ka	Comments	Rounded rate km ³ /ka
'Young' edifices									
Volcancillo	50?	150?	Un-glaciated dome in wide crater	< 50? (short lived)	0.33	0.39	0.006-0.007	likely shorter	0.006-0.01
Cabreria	56.5	< 130	Dome collapse block-and-ash flows	50 ?	4.13	4.91	0.082-0.098		0.08 - 0.10
Chachani	130 middle	222 base	Top not dated, craters preserved	90 - 130 max	30.34	33.20	0.275-0.302		0.27-0.31
Uyupampa	231	250?	Voluminous lava field	50 - 100?	2.36	2.72	0.031-0.036	likely shorter	0.03-0.04
El Rodado	239	< 400	Base not dated	200	6.26	9.17	0.031-0.045	likely shorter	0.03 - 0.05
La Horqueta	332	< 400	Older than Airport domes	100	3.24	6.46	0.032-0.064	likely shorter	0.03 - 0.07
Potrero domes	291	397	Dome cluster, short growth	100	11.22	12.53	0.112-0.125	likely shorter	0.11 - 0.13
El Angel	~400	463	Top not dated, crater preserved	60 - 100?	4.86	5.56	0.060-0.069	likely shorter	0.06 - 0.07
'Young' Edifices					63 ± 6.3	75 ± 7.5	Young volcano typical average eruption rate		0.07 - 0.09
< 640 Temporal gap > 463?						Estimated eruption rate over 500 kyr			0.12 - 0.15
'Old' edifices									
El Colorado	640	642	Two dome coulees	< 50 (short lived)?	4.13	6.16	0.082 - 0.123	likely shorter	0.08 - 0.13
Estribo	694	< 916	Overlies 1.4 Ma PDC (top IAI unit)	220 - 250?	59.35	63.03	0.252 - 0.268	likely longer	0.25 - 0.27
Nocarane	> 640	916	Top not dated; deeply eroded	175 - 200?	65.53	125.93	0.350 - 0.673	likely longer	0.35 - 0.70
Chingana	916 middle	1012	Top not dated; deeply eroded	80 - 100?	32.10	47.40	0.356 - 0.526	likely longer	0.35 - 0.60
C-LVC base	1012	1278 (Yura Tuff)	Lava flows	100 - 200	1.33	3.62	0.009 - 0.024	likely shorter	0.01 - 0.03
'Old' Edifices					162 ± 16	246 ± 24	Old volcano typical average eruption rate		0.21 - 0.34
						Estimated eruption rate over 600 kyr			0.27 - 0.41
Entire C-LVC volume					290 ± 29	350 ± 35	Eruption rate over 1100 kyr		0.26-0.31

Table 4. Results of calculation using morphometric parameters for the C-LVC and each of its edifices.

EDIFICE	ROCK TYPE	MAIN TEXTURE	MINERAL ASSEMBLAGE			OBSERVATIONS
			Crystal max. size	Pheno- and microphenocryst	Microlite in groundmass	
Pre-Chachani	Andesite	Microporph. Glomeroporph. vesiculated	2 mm	pl±cpx±(opx) (~23 %)	pl±cpx±mgt (~20%)	~10 % of vesicles. pl: sieve and overgrowth opx, cpx: dissolution surfaces
'OLD' EDIFICES GROUP						
Chachani Base	Andesite	Microporph.	2-4 mm	pl±cpx±amph pl±amp±bi (28-34%)	pl±cpx (30-34%)	sieve: pl patchy zoning: cpx breakdown: cpx, amph, rare ol
Chingana	Basaltic andesite	Microporph.	1 mm	pl±cpx±ol (~38 %)	pl±cpx±ol (~30 %)	intergrowth: plg-cpx sieve: pl; resorption: cpx, opx, pl, amph, ol
	Andesite	Microporph.	1-3 mm	pl±opx±cpx±amph (32-33%)	pl (26-30%)	2 types of pl; dissolution: pl, cpx intergrowth: pl-amph
Nocarane	Basaltic andesite	Porphyritic, glomeroporphyric	2 mm	pl±cpx±ol plg±opx±ol (aggregates)-(~21 %)	pl±cpx±ol (~31 %)	sieve: pl resorption: pl, cpx, opx
	Andesite	Porphyritic, poikilitic	4 mm	pl±amph±cpx (22-34 %)	pl±(cpx) (16-31%)	sieve: pl dissolution surf.: opx, cpx
	Dacite	Porphyritic	5 mm	pl±amph±bi (~24 %)	pl±(mgt) (~31%)	resorption: amph
Estribo	Dacite	Aphanitic, porphyritic	4 mm	plg±opx±amp (~22 %)	plg±px (~37%)	resorption: pl breakdown: opx intergrowth: pl et opx.
	Andesite	Vitrophyric, glomeroporphyric	5 mm	pl±cpx±amp (6-36%)	pl±mgt (21-61%)	sieve: pl breakdown: amph dissolution: bi
El Colorado	Andesite	Porphyritic, spherulitic	4 mm	plg±amp±bi (29-37 %)	pl±mgt (~12%)	devitrification of glass sieve and skeletal: pl patchy zoning: amph
'YOUNG' EDIFICES GROUP						
El Angel	Andesite	Porphyritic	6 mm	pl±amp±cpx±(biot) (~31%)	plg±cpx±oxy (~45%)	sieve, skeletal and overgrowth in pl; resorption: amph
El Rodado	Andesite	Porphyritic	2-6 mm	pl±cpx±(ol) (15-40%)	pl±cpx±(mgt) (26-52%)	sieve: pl breakdown: amph, rare ol.
La Horqueta	Andesite	Porphyritic	3-7 mm	pl±amp±bi±(cpx) pl±cpx±amph (30-45 %)	pl±amp±cpx±(mgt) (18-31 %)	sieve and dissolution: pl breakdown: amph, cpx, ol
Potrero Domes	Andesite	Porphyritic	4-6 mm	pl±amp±cpx±biot (~25 %)	plg±cpx (~46 %)	sieve: pl overgrowth: pl resorption: pl, cpx
	Dacite	Porphyritic	5-9 mm	pl±amp±(cpx) (24-39 %)	pl±px (29-49%)	sieve: pl, intergrowth: pl-amph resorption: px and bi breakdown: amph, bi
Uyupampa	Andesite	Porphyritic	3-5 mm	pl±amp±bi (30-42%)	pl±cpx±(ol) (20-43%)	sieve, overgrowth in pl

Chachani	Dacite	Porphyritic	3-5 mm	pl±opx±amp±(biot)	pl±opx	resorption and breakdown in amph resorption: pl, opx breakdown: amph
	Andesite	Porphyritic	3-5 mm	pl±amp±px (31-41 %)	pl±opx (20-50%)	sieve: pl dissolution: pl, amph, px breakdown: amph
La torta	Andesite	Porphyritic	6 mm	pl±px±ol±bi (~41 %)	Pl±px (~17 %)	dissolution: pl, bi, cpx breakdown: amph
Cabreria domes	Andesite	Aphyric	5 mm	Pl (~13 %)	pl±px (~15 %)	sieve: pl breakdown: amph
Volcancillo	Dacite	Porphyritic	5 mm	pl±amp±bi (~45 %)	pl±amp±px (~18 %)	sieve: pl resorption: pl and bi breakdown: bi

Table 5. Petrographic characteristics of lavas from the twelve C-LVC edifices, and of Pre-Chachani and Chachani base lavas. Pl: plagioclase, opx: orthopyroxene, cpx: clinopyroxene, amph: amphibole, bi: biotite, mgt: magnetite. % values in parentheses represents the percentage of crystal content as phenocrysts (>500 μm) and microphenocrysts (100-500 μm) and microlites (<100 μm) in the groundmass.